Solid-State Electrochemical Thermal Transistors

*Qian Yang, Hai Jun Cho, Zhiping Bian, Mitsuki Yoshimura, Joonhyuk Lee, Hyoungjeen Jeen, Jinghuang Lin, Jiake Wei, Bin Feng, Yuichi Ikuhara, and Hiromichi Ohta**

Q. Yang, Z. Bian, M. Yoshimura
Graduate School of Information Science and Technology, Hokkaido University, N14W9, Kita, Sapporo 060-0814, Japan

Q. Yang
Present address: Institute of Quantum and Sustainable Technology (IQST), School of Chemistry and Chemical Engineering, Jiangsu University, Zhenjiang 212013, China

H. J. Cho, H. Ohta
Research Institute for Electronic Science, Hokkaido University, N20W10, Kita, Sapporo 001-0020, Japan
E-mail: hiromichi.ohta@es.hokudai.ac.jp

H. J. Cho
Present address: Department of Mechanical Engineering, University of Ottawa, 161 Louis Pasteur. Ottawa, ON K1N 6N5, Canada

J. Lee, H. Jeen
Department of Physics, Pusan National University, Geumjeong-gu, Busan 46241, Korea

J. Lin, J. Wei, B. Feng, Y. Ikuhara
Institute of Engineering Innovation, The University of Tokyo, 2-11-16 Yayoi, Bunkyo, Tokyo 113-8656, Japan

J. Wei
Present address: Department of Analytical Chemistry, Dalian Institute of Chemical Physics, 457 Zhongshan Road, Dalian 116023, China

Keywords: thermal transistor, electrochemistry, redox, solid-state, thermal conductivity, transition metal oxide

Thermal transistors that electrically control heat flow have attracted growing attention as thermal management devices and phonon logic circuits. Although several thermal transistors have been demonstrated, the use of liquid electrolytes may limit the application from the viewpoint of reliability or liquid leakage. Here, we demonstrate a solid-state thermal transistor that can electrochemically control the heat flow with an on-to-off ratio of the thermal conductivity (κ) of ~4 without using any liquid. The thermal transistor is a multilayer film composed of an upper electrode, strontium cobaltite ($SrCoO_x$), solid electrolyte, and bottom electrode. An electrochemical redox treatment at 280 °C in air repeatedly modulates the crystal structure and κ of the $SrCoO_x$ layer. The fully oxidized perovskite-structured $SrCoO_3$ layer shows a high κ ~3.8 W m^{-1} K^{-1}, whereas the fully reduced defect perovskite-structured $SrCoO_2$ layer shows a low κ ~0.95 W m^{-1} K^{-1}. The present solid-state electrochemical thermal transistor may become next-generation devices toward future thermal management technology.

1. Introduction

Thermal transistors[1-3], which can electrically control heat flow, have attracted growing attention as thermal management devices[4] and phonon logic circuits[5, 6]. A thermal transistor is composed of an active material and a switching material. The active material shows nonlinear heat transport properties upon a phase change, while the switching material controls the phase of the active material repeatedly. Thus, switching electrically modulates the thermal conductivity (κ) of the active material.

History of thermal transistor development is short, only less than ten years. In 2014, Ben-Abdallah and Biehs theoretically predicted a thermal transistor that uses the metal-to-insulator transition (MIT) of VO_2 [7] as the active layer. According to the Wiedemann-Frantz law, metallic VO_2 exhibits κ that is at least ~1 W m^{-1} K^{-1} higher than the insulator VO_2 due to the electron contribution. That is, $\kappa_{ele} = L \cdot \sigma \cdot T$, where L is the Lorentz number (2.44×10^{-8} W Ω K^{-2}), σ is the electrical conductivity (~1500 S cm^{-1} for metal phase VO_2[8]), and T is the absolute temperature. Since the MIT occurs at ~68 °C in the bulk state, they predicted that κ of the VO_2 layer can be switched by Joule heating of the VO_2 layer above 68 °C. However, in

2017, Lee *et al*.[9] reported that the Wiedemann-Franz law was not applicable to VO_2 and the κ values of VO_2 before and after the MIT were almost the same[10]. Although Zhu *et al*.[11] demonstrated a thermal rectification in VO_2 beams, the value is not sufficient for thermal transistor applications. Consequently, the thermal transistor described in Ref. [7] is impossible to realize.

Recently, electrochemical control of κ for materials using liquid electrolytes has attracted attention. Cho *et al*.[12] realized the first thermal transistor in 2014. They measured κ of a $LiCoO_2$ thin film before and after electrochemical delithiation using the time-domain thermo-reflectance (TDTR) method. κ of the $LiCoO_2$ film can be reversibly modulated in the range of ~5.4–3.7 W m^{-1} K^{-1}. To date, several similar thermal transistors have been proposed. In 2018, Sood *et al*.[13] demonstrated that the electrochemical Li intercalation/deintercalation using a liquid electrolyte modulates κ of MoS_2. In 2020, transition metal oxide (TMO)-based thermal transistors using an ionic liquid as the electrolyte have been reported[14, 15]. Lu *et al*.[15] used $SrCoO_x$ as the active layer. The κ ratio of oxidized $SrCoO_3$ (κ = 4.33 ±1.62 W m^{-1} K^{-1}) vs. protonated $HSrCoO_{2.5}$ (κ = 0.44 ±0.06 W m^{-1} K^{-1}) is 10±4. Very recently, Zhou *et al*.[16] reported a heat conductor–insulator transition in electrochemical hybrid superlattices composed of MoS_2 and an organic molecule. These thermal transistors utilize the change in κ of the active material when ions are intercalated/deintercalated electrochemically. Although these materials show suitable thermal transistor characteristics, the use of liquids (electrolyte, ionic liquid) may limit the application because such devices must be placed in containers and sealed. Thus, the development of solid-state thermal transistors is crucial.

To realize solid-state thermal transistors, we used a solid electrolyte, yttria-stabilized zirconia (YSZ), though the operation temperature is a bit high (~300 °C) compared to the liquid electrolyte. We choose YSZ from the following reasons. YSZ is an oxide (O^{2-}) ion conductor and has been applied as the solid electrolyte for solid oxide fuel cells (SOFCs)[17]. Additionally, rather large-sized YSZ single crystals are commercially available. Most importantly, many perovskite-related TMOs are heteroepitaxially grown on YSZ single crystal substrates.[18-20]

In this study, we focus on $SrCoO_x$ ($2 \leq x \leq 3$) as the active material for a solid-state electrochemical thermal transistor. $SrCoO_x$ is known as an oxygen sponge, and the O^{2-} ion concentration of $SrCoO_x$ can be controlled at relatively low temperatures[21-24]. Our

preliminary studies (**Supporting Information S1**, **Figs. S1−S6, Table S1**) reveal that a $SrCoO_{2.5}$ film with a brownmillerite (BM) structure grown on YSZ is electrochemically oxidized into a perovskite (P-) $SrCoO_3$ film, which shows a high σ of ~1400 S cm^{-1} [25]. Moreover, we found that a $SrCoO_{2.5}$ film on YSZ can be electrochemically reduced into a defect perovskite (DP-) $SrCoO_2$ film that shows highly insulating. Generally, κ of material is expressed as the summation of κ due to the quantized lattice vibration (phonon) and κ due to the electron[26]. The former depends on the crystal structure and quality. The latter is given by the Wiedemann-Franz law as described above. From these observations, we expect that κ of P-$SrCoO_3$ is higher than that of DP-$SrCoO_2$, as schematically illustrated in **Fig. 1**.

Here, we demonstrate a solid-state electrochemical thermal transistor. The thermal transistor consists of a multilayered structure composed of a Pt upper electrode, a $SrCoO_{2.5}$ active layer, a solid electrolyte Gd-doped CeO_2 layer on a YSZ substrate, and a Pt bottom electrode on the backside of the YSZ. The multilayer sample is placed on a heater stage and heated to 280 °C in air. Then electrochemical oxidation/reduction treatment at 280 °C in air repeatedly modulates the crystal structure and κ of the $SrCoO_x$ layer. The fully oxidized P-$SrCoO_3$ layer shows a high κ ~3.8 W m^{-1} K^{-1}. By contrast, the fully reduced DP-$SrCoO_2$ layer shows a low κ ~0.95 W m^{-1} K^{-1}. Consequently, a solid-state thermal transistor electrochemically controls the heat flow with an on-to-off κ ratio of ~4.

2. Results and Discussion

First, we fabricated solid-state electrochemical thermal transistors (**Supporting Information S2**, **Fig. S7, S8**). Then, a fabricated solid-state electrochemical thermal transistor (5 mm × 5 mm) was set on a Pt-coated glass substrate (**Supporting Information S3**, **Fig. S9**). After heating to 280 °C in air, an electrochemical redox treatment was performed by applying a constant current of −50 μA for reduction and +50 μA for oxidation. We controlled the current application time by monitoring the flown electron density $Q = (I \cdot t)/(e \cdot V)$, where I is the flown current, t is the applied time, e is the electron charge, and V is the volume of the $SrCoO_{2.5}$ film (5 mm × 5 mm × ~50 nm). After applying the current, the device was immediately cooled to room temperature.

The electrochemical redox treatment began by applying a negative current to reduce BM-$SrCoO_{2.5}$ into DP-$SrCoO_2$ (**Fig. 2a**). Initially, the dc voltage in the electrochemical reduction was ~ −5.1 V, which was close to that expected from the dc resistance of the YSZ substrate

(~100 kΩ, 5 mm × 5 mm × 0.5 mm) (**Supporting Information S3**, **Fig. S10**). Two semicircles of ~100 kΩ and ~25 kΩ were observed when we measured the impedance spectroscopy (Cole-Cole plot, data not shown). The former indicates resistance of YSZ substrate and the latter indicates the YSZ/Pt interface resistance. As Q increased, the absolute value of the voltage gradually increased and became saturated around −5.7 V. Then it jumped to −6.1 V and became saturated again when Q was ~1.7×10^{22} cm^{-3}. This change in the voltage corresponds to the electrochemical reduction of BM-$SrCoO_{2.5}$ as $SrCoO_{2.5} + e^- \rightarrow SrCoO_2 + 0.5O^{2-}$, which was confirmed by the change in the XRD patterns (**Figs. 3a–3c**). Afterward, the voltage gradually increased with Q but dramatically decreased once Q exceeded ~3.2×10^{22} cm^{-3}. Electrochemical reduction of GDC[27] occurred after the over-reduction treatment (data not shown). It should be noted that GDC is easily oxidized during electrochemical oxidation.

Separately, we measured the κ of the $SrCoO_x$ layer by the TDTR method using the top Pt electrode as the transducer (**Figures S15**, **S16**). The TDTR measurement was performed at room temperature in air. **Figure 2b** shows the TDTR decay curves upon electrochemical reduction (See also **Fig. S17**). Compared to the as-grown state (0 cm^{-3}), the decay slowed as Q increased, suggesting a decrease of κ of the $SrCoO_x$ layer. **Figure 2c** plots the estimated κ as a function of Q. κ of as-grown BM-$SrCoO_{2.5}$ was ~1.9 W m^{-1} K^{-1} but gradually decreased with Q. When Q reached ~1.7×10^{22} cm^{-3}, κ became saturated at ~1 W m^{-1} K^{-1}.

Next the device was oxidized electrochemically (**Fig. 2d**). The initial dc voltage was ~4.0 V. As Q increased, the voltage increased gradually and became saturated at ~4.2 V. When Q exceeded ~1.7×10^{22} cm^{-3}, the voltage dramatically increased and became saturated at ~4.8 V when Q reached ~3.4×10^{22} cm^{-3}.

The change in the crystalline phases is as follows:
(Up to ~1.7×10^{22} cm^{-3}) $SrCoO_2 + 0.5O^{2-} \rightarrow SrCoO_{2.5} + e^-$
(Up to ~3.4×10^{22} cm^{-3}) $SrCoO_{2.5} + 0.5O^{2-} \rightarrow SrCoO_3 + e^-$

The XRD patterns confirmed these changes (**Figs. 3c−3e**). These results reveal that the x value in $SrCoO_x$ can be controlled electrochemically between 2 and 3 without destroying the crystal structure.

The TDTR decay became faster as Q increased (**Fig. 2e**), suggesting κ of the $SrCoO_x$ layer increased. **Figure 2f** shows two stepwise increases of κ of the $SrCoO_x$ at Q ~1.7×10^{22} cm^{-3} and ~3.4×10^{22} cm^{-3}. These stepwise increases of κ correspond to the oxidation from DP-$SrCoO_2$ to BM-$SrCoO_{2.5}$ and from BM-$SrCoO_{2.5}$ to P-$SrCoO_3$. The κ of fully oxidized P-$SrCoO_3$ was ~3.5 W m^{-1} K^{-1}. These results reveal that κ of the $SrCoO_x$ layer can be controlled electrochemically between ~1 W m^{-1} K^{-1} and ~3.5 W m^{-1} K^{-1} using YSZ as the solid electrolyte.

Finally, we examined the repeatability of the thermal transistor. **Figure 4** shows the change in the crystal lattice of $SrCoO_x$ layer on the redox treatment. In the out-of-plane XRD patterns, the diffraction peak around 5.05 nm^{-1} was 008 for the as-grown BM-$SrCoO_{2.5}$. The reduction treatment shifted the diffraction peak to ~5.4 nm^{-1} (002 DP-$SrCoO_2$), while the oxidation treatment shifted it to ~5.25 nm^{-1} (002 P-$SrCoO_3$). Repeating the redox treatments ten times did not change the peak position or shape except for the first reduction and oxidation treatments. Similarly, the applied voltage was almost unchanged in each redox cycle except for the first reduction and oxidation treatments (**Fig. S11**). **Figure 4b** shows the change in the d-value of reduced DP-$SrCoO_2$ and oxidized P-$SrCoO_3$ layers upon redox cycles. The extracted lattice parameter c was 0.3706 nm for reduced DP-$SrCoO_2$ and 0.3795 nm for oxidized P-$SrCoO_3$. These results reveal that the crystal structure is maintained after redox cycling.

Figure 5 shows the change in the TDTR decay curves of the redox-cycled device. The TDTR decay of oxidized P-$SrCoO_3$ was always faster than that of reduced DP-$SrCoO_2$. Using these TDTR decay curves, the change in κ of reduced DP-$SrCoO_2$ and oxidized P-$SrCoO_3$ layers were simulated in the redox cycles (See **Fig. S18**). The average κ values were 0.95 W m^{-1} K^{-1} for reduced DP-$SrCoO_2$ and 3.8 W m^{-1} K^{-1} for oxidized P-$SrCoO_3$, indicating an on-to-off thermal conductivity ratio for the $SrCoO_x$ layer of 4. If we assume that the electron contribution of the κ_{ele} of P-$SrCoO_3$ in the cross-plane direction by the Wiedemann-Frantz law using the in-plane electrical conductivity (~590 S cm^{-1}, **S1.3**), the value is ~0.43 W m^{-1} K^{-1} (~11% of the observed κ). These results indicate the on-to-off thermal conductivity ratio mainly comes from the difference between DP and P structure of $SrCoO_x$.

Here, we compare the characteristics of the present solid-state electrochemical thermal transistor with the reported liquid-based electrochemical thermal transistors (**Table 1**). The

present solid-state thermal transistor shows comparable characteristics except that the operating temperature is high due to low oxide ion conductivity of YSZ crystal. In order to overcome this problem, reduction of the resistance of the solid electrolyte is crucial.

If we except the problem of high operating temperature, the present solid-state electrochemical thermal transistor has several advantages compared to liquid-based electrochemical thermal transistors. First, it does not need to be placed in a container and sealed. Second, it shows stable operations after repeated cycles. Third, it has a good reproducibility. The multilayered structure composed of Pt, $SrCoO_x$, GDC, and YSZ is maintained after the redox cycles (**Figs. S12**, **S13**), and the crystal structure of $SrCoO_x$ maintains the perovskite structure upon the redox reaction (**Fig. S14**). We fabricated many thermal transistors (>20 pieces) and tested the cycle properties. And we confirmed that all the devices show the on/off ratio of ~4 between the fully oxidized perovskite $SrCoO_3$ vs the reduced defect perovskite $SrCoO_2$. Fourth, the device operations obey Faraday's law of electrolysis without current leakage. Thus, controlling Q can realize on/off control of the device. In the present device, the solid-electrolyte (0.5-mm-thick YSZ crystal) and the solid-electrolyte/Pt interface dominate the current flow. In other word, use of a solid-electrolyte with a higher O^{2-} ion conductivity or reducing the thickness of a solid-electrolyte is effective to reduce the operating temperature and switching time of the device.

3. Conclusions

In summary, we demonstrated a solid-state electrochemical thermal transistor without any liquid that can control the heat flow using the change in the thermal conductivity of the $SrCoO_x$ layer. The on-to-off ratio of the thermal conductivity (κ) was ~4. The solid-state electrochemical thermal transistor was composed of the upper electrode, $SrCoO_x$, the solid electrolyte, and the bottom electrode. The electrochemical redox treatment at 280 °C in air turned the thermal transistor on and off and repeatedly modulates the crystal structure and κ of the $SrCoO_x$ layer. When the thermal transistor was on, κ of the $SrCoO_3$ layer was ~3.8 W m^{-1} K^{-1}. By contrast, κ of the $SrCoO_2$ layer was ~0.95 W m^{-1} K^{-1} when it was off. Additionally, we confirmed the cycle properties of the thermal transistor (10 cycles).

Although the present solid-state thermal transistor shows comparable characteristics with liquid-based thermal transistors ever reported, the operating temperature is high due to low oxide ion conductivity of YSZ crystal. In order to develop practical thermal transistors,

reduction of the resistance of the solid electrolyte is crucial. When this problem is solved, the present solid-state electrochemical thermal transistor may become next-generation devices toward future thermal management technology such as electric heat shutters.

4. Experimental Section

Fabrication of the thermal transistors: $SrCoO_{2.5}$ films were heteroepitaxially grown on 10%-Gd-doped CeO_2 (GDC) buffered (001)-oriented YSZ substrates by pulsed laser deposition (PLD) technique. First, ~10-nm-thick GDC was heteroepitaxially grown on a YSZ (10 mm × 10 mm × 0.5 mm, double-sided polished, Crystal Base) substrate at 750 °C in an oxygen atmosphere (10 Pa). Focused KrF excimer laser pulses (λ = 248 nm, fluence ~2 J cm^{-2} $pulse^{-1}$, repetition rate = 10 Hz) were irradiated onto the ceramic target of GDC. Subsequently, a ~50-nm-thick $SrCoO_{2.5}$ film was heteroepitaxially grown on the GDC film at 750 °C in an oxygen atmosphere (10 Pa). The laser fluence was ~2 J cm^{-2} $pulse^{-1}$. After film growth, the sample was cooled to room temperature in the PLD chamber in an oxygen atmosphere (10 Pa). Then ~60-nm-thick Pt film was sputtered on the top surface of the $SrCoO_{2.5}$ epitaxial film followed by ~40-nm-thick Pt film sputtering on the backside of the YSZ substrate. Pt sputtering was performed at room temperature. Finally, the sample was cut into four squares (5 mm × 5 mm).

Electrochemical redox treatments: The thermal transistor (5 mm × 5 mm) was put on a Pt-coated glass substrate, which was heated at 280 °C in air. Then the electrochemical redox treatment was performed by applying a constant current of ±50 μA. After applying the current, the sample was immediately cooled to room temperature.

Crystallographic analyses: The crystalline phase, orientation, and lattice parameters of the resultant films were analyzed by high-resolution X-ray diffraction (Cu $K\alpha_1$, λ = 1.54059 Å, ATX-G, Rigaku). The out-of-plane and in-plane Bragg diffraction patterns as well as the rocking curves were measured at room temperature to clarify the changes in the crystalline phase of $SrCoO_x$. The lattice parameters were calculated from the diffraction peaks. Atomic force microscopy (AFM, Nanocute, Hitachi Hi-Tech Sci. or MFP-3D Origin, Oxford Instruments) was used to observe the surface morphology of the films at room temperature. The atomic arrangement of the $SrCoO_x$ films were visualized using scanning transmission electron microscopy (STEM, JEM-ARM200CF, JEOL) operating at 200 keV.

X-ray absorption spectroscopy (Fig. S6): Soft X-ray absorption spectroscopy (XAS) of the Co L- and O K-edges was performed at the 2A beamline in the Pohang Accelerator Laboratory. The direction of the incident X-rays was normal to the sample plane, and a circular polarization was used. The XAS spectra of these samples were measured in the total electron yield (TEY) mode at room temperature. The base pressure of the system was 10^{-9} Torr.

Measurements of the optical and electrical properties (Fig. S5, Table S1): After mechanically removing the Ag paste film from the backside of the YSZ substrate, the optical transmission spectra of the samples were acquired at room temperature using a UV–VIS–NIR spectrometer (SolidSpec-3700, Shimadzu). The electrical resistivities of the resultant films were measured by the dc four-probe method with van der Pauw electrode configuration.

Measurements of the thermal conductivity: κ of the $SrCoO_x$ films perpendicular to the substrate surface was measured by time-domain thermoreflectance (TDTR, PicoTR, PicoTherm). The top Pt film was used as the transducer. The decay curves of the TDTR signals were simulated to obtain κ. The specific heat capacities of the layers used for the TDTR simulation were Pt, 132 J kg^{-1} K^{-1}; $SrCoO_x$, 485 J kg^{-1} K^{-1}; and YSZ, 460 J kg^{-1} K^{-1}. Details of the TDTR method are described in the Supporting Information (S4) and elsewhere.[28-30] Regarding the treatment of the thermal conductivity values, since there are several uncertainties such as position of the baseline, position of the time zero, and noise of the signal, we used the error bars of ±10% of the obtained values.

Table 1. Thermal transistor characteristics of the reported electrochemical thermal transistors. Compared with the liquid electrolyte or ionic liquid based thermal transistors, the present solid-state thermal transistor shows comparable characteristics except that the operating temperature is high.

Active material	Electrolyte	On/off ratio	Operating temperature (°C)	Operating voltage (V)	Switching time	Ref.
$LiCoO_2/Li_{0.6}CoO_2$	$LiClO_4$-EC/DMC (Liquid)	~1.5	RT	4.2	~1.5 h	[12]
$MoS_2/LiMoS_2$	$LiPF_6$-EC/DEC (Liquid)	~10	RT	3	7 min	[13]
$La_5Ca_9Cu_{24}O_{41}$	DEME-TFSI (Ionic liquid)	~4	RT	2	~0.5 h	[14]
$SrCoO_3/HSrCoO_{2.5}$	HMIM-TFSI (Ionic liquid)	~10	RT	4	~0.5 h	[15]
MoS_2/MoS_2-$C_{16}H_{33}N(CH_3)_3Br$	$C_{16}H_{33}N(CH_3)_3Br$ -NMP (Liquid)	~80	RT	~3	~2.3 min	[16]
$SrCoO_3/SrCoO_2$	GDC/YSZ (Solid-state)	~4	280	~6.5	~3 min	This work

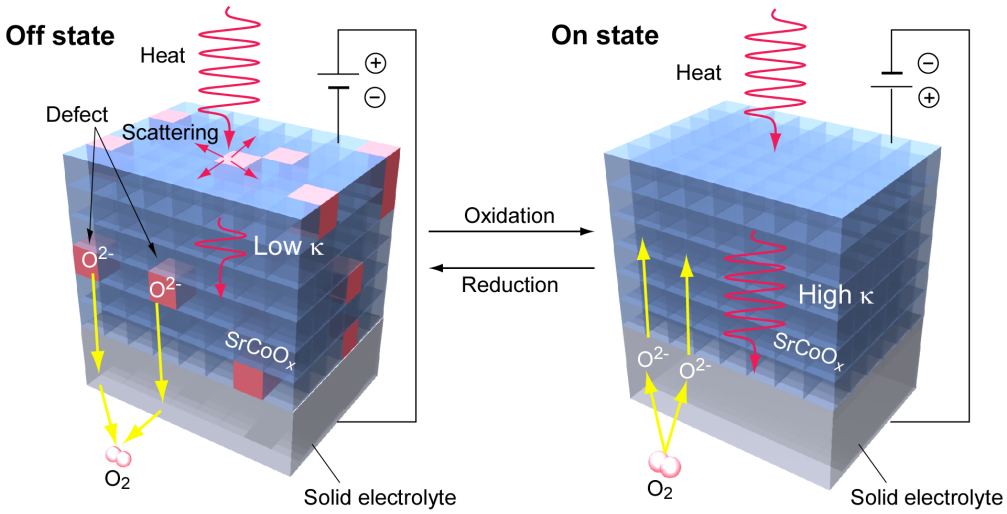

Figure 1. Design of a solid-state electrochemical thermal transistor. (Left) Off state. Oxygen defects are generated in the $SrCoO_x$ layer via the electrochemical reduction treatment. Resultant $SrCoO_2$ layer (defect perovskite) contains 1/3 oxygen defects against $SrCoO_3$, and the defects scatter the heat flow, reducing the thermal conductivity. (Right) On state. Electrochemical oxidation treatment causes the oxygen defects to disappear, increasing the thermal conductivity.

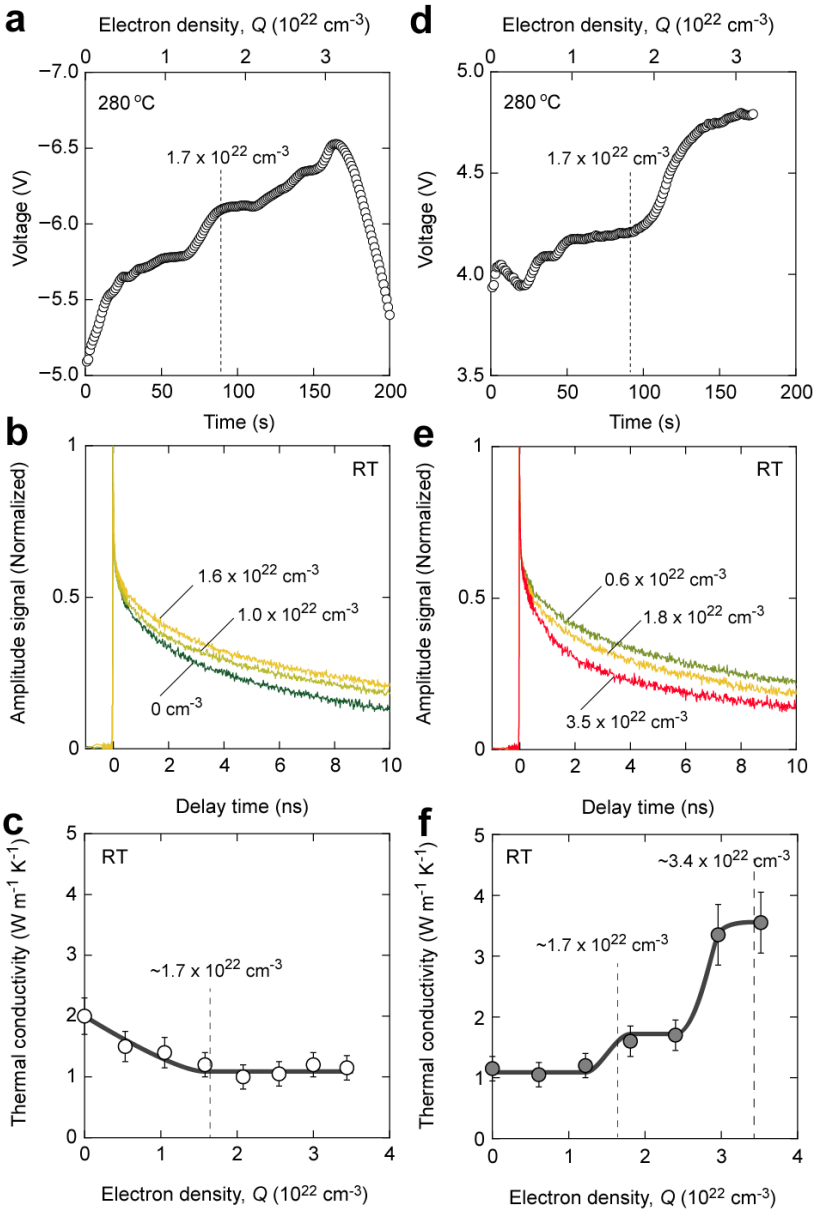

Figure 2. Operation of a solid-state thermal transistor. a, d) Changes in the observed dc voltage of the thermal transistor during (a) reduction from $SrCoO_{2.5}$ to $SrCoO_2$ and (d) oxidation from $SrCoO_2$ to $SrCoO_3$. Dotted lines indicate the theoretical electron density for the redox reaction of $SrCoO_2$/$SrCoO_{2.5}$/$SrCoO_3$. If Q exceeds ~3 × 10^{22} cm^{-3}, the voltage drops due to the reduction of GDC. b, e) Changes in the TDTR decay curves of the thermal transistor after (b) reduction and (e) oxidation treatments. c, f) Changes in the thermal conductivity of the $SrCoO_x$ layer after (c) reduction and (f) oxidation. Thermal conductivity of the $SrCoO_{2.5}$ layer for as-fabricated thermal transistor (0 cm^{-3}) is ~1.8 W m^{-1} K^{-1}. TDTR decay is gradually suppressed as the electron density increases. Thermal conductivity of the $SrCoO_x$ layer gradually decreases with Q and becomes constant (~1 W m^{-1} K^{-1}) when Q exceeds 1.7 × 10^{22} cm^{-3}. c, d) Changes in (c) the TDTR decay curves and (d) the thermal

conductivity of a thermal transistor with oxidation. Thermal conductivity changes from ~1 W m^{-1} K^{-1} to ~3.5 W m^{-1} K^{-1}.

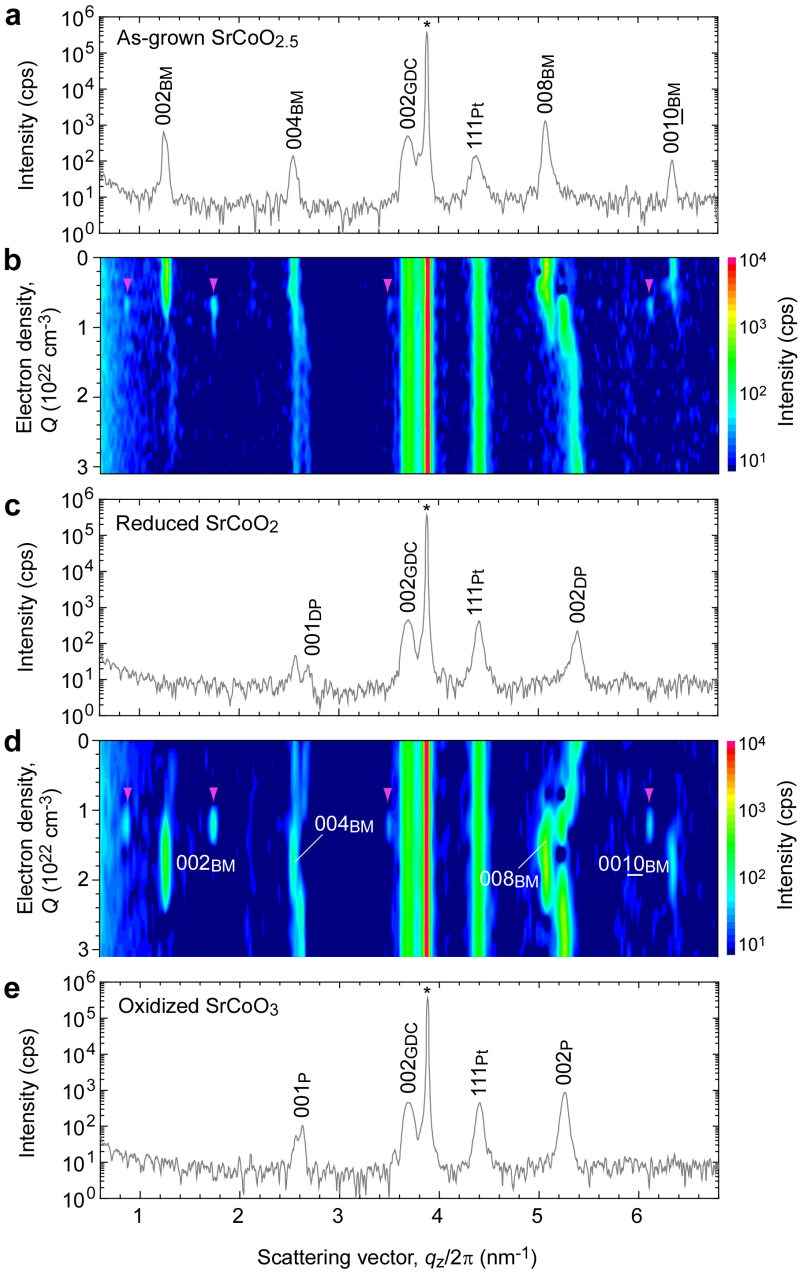

Figure 3. Topotactic crystal structure change of the $SrCoO_x$ film upon electrochemical reduction/oxidation treatment. a, c, e) Out-of-plane XRD patterns for (a) the as-grown $SrCoO_{2.5}$, (c) reduced $SrCoO_2$, and (e) oxidized $SrCoO_3$. a) Intense diffraction peaks of 00*l* (*l* = 2, 4, 8, and 10) brownmillerite (BM) $SrCoO_{2.5}$ are seen together with those of 002 GDC, 002 YSZ (*) and 111 Pt. c) Intense diffraction peaks of 00*l* (*l* = 1 and 2) defect perovskite (DP) $SrCoO_2$ are seen together with 002 GDC, 002 YSZ (*) and 111 Pt. e) Intense diffraction peaks of 00*l* (*l* = 1 and 2) perovskite (P) $SrCoO_3$ are seen together with 002 GDC, 002 YSZ (*) and 111 Pt. b, d) Changes in the out-of-plane XRD patterns of (b) $SrCoO_{2.5}$ upon reduction and (d) $SrCoO_2$ upon oxidation. b) Diffraction peaks of BM disappear when Q exceeds 0.8×10^{22} cm^{-3} and the intermediate phase appears (arrows). Intermediate phase

peaks disappear and 002 DP-$SrCoO_2$ with defect perovskite structure appears. d) Diffraction peaks of DP disappear when Q exceeds 1.0×10^{22} cm^{-3}, while the intermediate phase appears (arrows). Then these intermediate phase peaks disappear and the BM phase appears. Finally, P-$SrCoO_3$ appears when Q exceeds 2.4×10^{22} cm^{-3}.

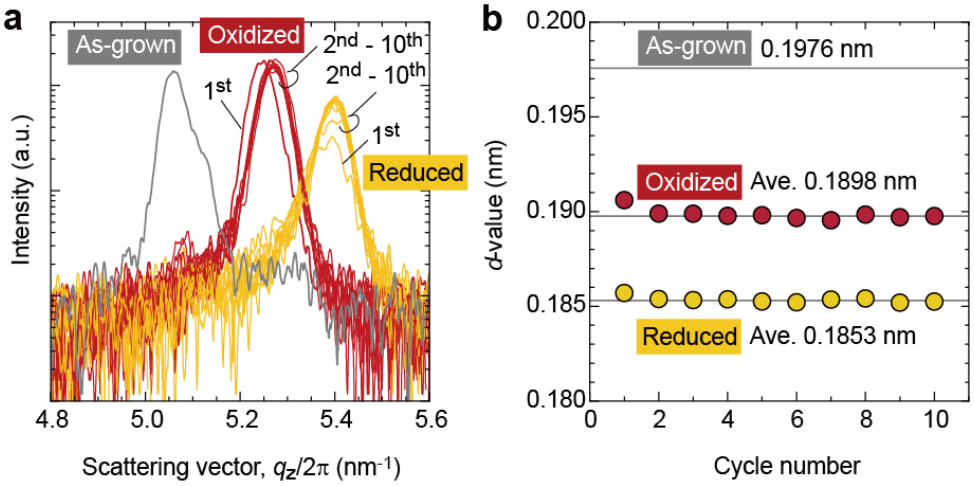

Figure 4. Repeatable change in the crystal lattice of $SrCoO_x$ layer on the redox treatment. a) Change in the out-of-plane XRD patterns in the $q_z/2\pi$ range of 4.8–5.6 nm^{-1}. Diffraction peak around 5.05 nm^{-1} is 008 of $SrCoO_{2.5}$. Diffraction peak shifts to ~5.4 nm^{-1} (002 $SrCoO_2$) after the reduction treatment, while oxidation treatment shifts to ~5.25 nm^{-1} (002 $SrCoO_3$). Upon repeating the redox treatments 10 times, the peak position and shape are unchanged except for the 1st reduction and oxidation treatments. b) Change in the *d*-value of the reduced $SrCoO_2$ and oxidized $SrCoO_3$ layers upon redox cycles. Extracted lattice parameter *c* is 0.3706 nm for reduced $SrCoO_2$ and 0.3795 nm for oxidized $SrCoO_3$.

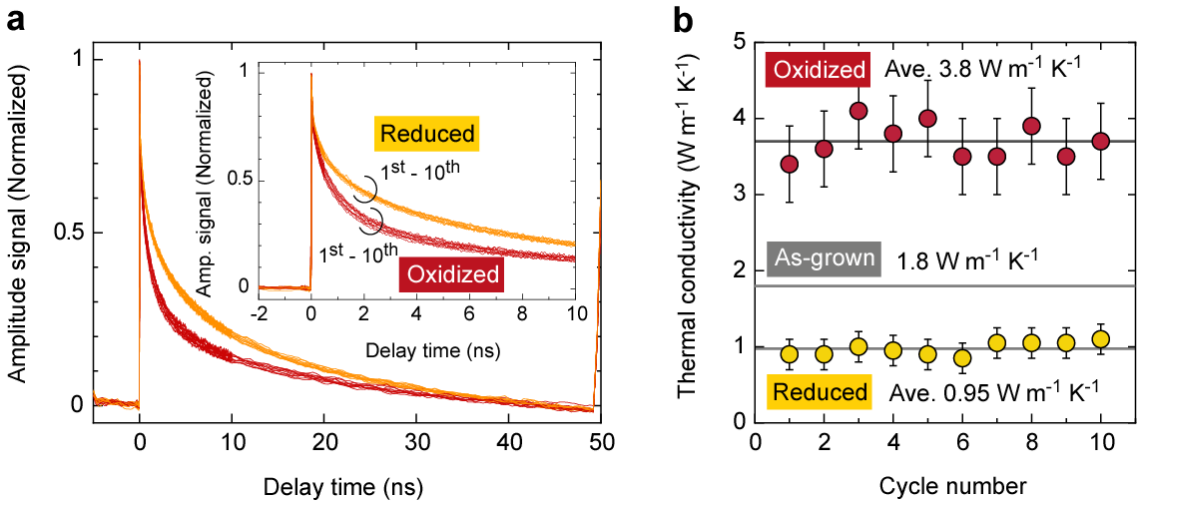

Figure 5. Repeatable change in the thermal conductivity of $SrCoO_x$ layer on the redox treatment. a) Change in the TDTR decay curves. TDTR decay of oxidized $SrCoO_3$ is always faster than that of reduced $SrCoO_2$. Good repeatability is seen. b) Change in the thermal conductivity of reduced $SrCoO_2$ and oxidized $SrCoO_3$ layers upon redox cycles. Average thermal conductivity is 0.95 W m^{-1} K^{-1} for reduced $SrCoO_2$ and 3.8 W m^{-1} K^{-1} for oxidized $SrCoO_3$. On/off thermal conductivity ratio of $SrCoO_x$ layer is 4.

Supporting Information

Supporting Information is available from the Wiley Online Library or from the author.

S1. Solid-state electrochemical redox treatment of $SrCoO_x$ (x = 2, 2.5, and 3) films

S2. Fabrication of the thermal transistors

S3. Detailed thermal transistor operations

S4. Thermal conductivity measurement of the thermal transistors

Acknowledgements

This research was supported by Grants-in-Aid for Scientific Research A (22H00253) and Innovative Areas (19H05791 and 19H05788) from the Japan Society for the Promotion of Science (JSPS). Part of this work was supported by the Crossover Alliance to Create the Future with People, Intelligence and Materials, and by the Network Joint Research Center for Materials and Devices. Part of this work was supported by and the Advanced Research Infrastructure for Materials and Nanotechnology Japan (Grant Number JPMXP1222UT0055) by Ministry of Education, Culture, Sports, Science and Technology (MEXT). Q.Y. was supported by a Grant-in-Aid for JSPS Fellows (21J10042). Z.B. was supported by Hokkaido University DX Doctoral Fellowship.

Received: ((will be filled in by the editorial staff))
Revised: ((will be filled in by the editorial staff))
Published online: ((will be filled in by the editorial staff))

References

[1] B. W. Li, L. Wang, G. Casati, *Appl. Phys. Lett.* **2006**, *88*, 143501.

[2] G. Wehmeyer, T. Yabuki, C. Monachon, J. Q. Wu, C. Dames, *Appl. Phys. Rev.* **2017**, *4*, 041304.

[3] T. Swoboda, K. Klinar, A. S. Yalamarthy, A. Kitanovski, M. M. Rojo, *Adv. Electron. Mater.* **2021**, *7*, 2000625.

[4] C. Acar, I. Dincer, *Energy Storage* **2019**, *1*, e47.

[5] L. Wang, B. Li, *Phys. Rev. Lett.* **2007**, *99*, 177208.

[6] S. R. Sklan, *AIP Adv.* **2015**, *5*, 053302.

[7] P. Ben-Abdallah, S. A. Biehs, *Phys. Rev. Lett.* **2014**, *112*, 044301.

[8] M. Nakano, K. Shibuya, D. Okuyama, T. Hatano, S. Ono, M. Kawasaki, Y. Iwasa, Y. Tokura, *Nature* **2012**, *487*, 459-462.

[9] S. Lee, K. Hippalgaonkar, F. Yang, J. W. Hong, C. Ko, J. Suh, K. Liu, K. Wang, J. J. Urban, X. Zhang, C. Dames, S. A. Hartnoll, O. Delaire, J. Q. Wu, *Science* **2017**, *355*, 371.

[10] C. N. Berglund, H. J. Guggenheim, *Phys. Rev.* **1969**, *185*, 1022-1033.

[11] J. Zhu, K. Hippalgaonkar, S. Shen, K. V. Wang, Y. Abate, S. Lee, J. Q. Wu, X. B. Yin, A. Majumdar, X. Zhang, *Nano Lett.* **2014**, *14*, 4867-4872.

[12] J. Cho, M. D. Losego, H. G. Zhang, H. Kim, J. M. Zuo, I. Petrov, D. G. Cahill, P. V. Braun, *Nat. Commun.* **2014**, *5*, 4035.

[13] A. Sood, F. Xiong, S. D. Chen, H. T. Wang, D. Selli, J. S. Zhang, C. J. McClellan, J. Sun, D. Donadio, Y. Cui, E. Pop, K. E. Goodson, *Nat. Commun.* **2018**, *9*, 4510.

[14] N. Terakado, Y. Nara, Y. Machida, Y. Takahashi, T. Fujiwara, *Sci. Rep.* **2020**, *10*, 14468.

[15] Q. Y. Lu, S. Huberman, H. T. Zhang, Q. C. Song, J. Y. Wang, G. Vardar, A. Hunt, I. Waluyo, G. Chen, B. Yildiz, *Nature Mater.* **2020**, *19*, 655-662.

[16] J. W. Zhou, Y. C. Wu, H. D. Kwon, Y. B. Li, X. Xiao, Y. S. Ye, Y. X. Ma, K. E. Goodson, H. Y. Hwang, Y. Cui, *Nano Lett.* **2022**, *22*, 5443-5450.

[17] E. D. Wachsman, K. T. Lee, *Science* **2011**, *334*, 935-939.

[18] H. Jeen, Z. H. Bi, W. S. Choi, M. F. Chisholm, C. A. Bridges, M. P. Paranthaman, H. N.

Lee, *Adv. Mater.* **2013**, *25*, 6459-6463.

[19] Q. Yang, H. J. Cho, H. Jeen, H. Ohta, *J. Appl. Phys.* **2021**, *129*, 215303.

[20] X. Zhang, G. Kim, Q. Yang, J. K. Wei, B. Feng, Y. Ikuhara, H. Ohta, *ACS Appl. Mater. Interfaces* **2021**, *13*, 54204-54209.

[21] H. Jeen, W. S. Choi, M. D. Biegalski, C. M. Folkman, I. C. Tung, D. D. Fong, J. W. Freeland, D. Shin, H. Ohta, M. F. Chisholm, H. N. Lee, *Nature Mater.* **2013**, *12*, 1057-1063.

[22] T. Katase, Y. Suzuki, H. Ohta, *Adv. Electron. Mater.* **2016**, *2*, 1600044.

[23] N. Lu, P. Zhang, Q. Zhang, R. Qiao, Q. He, H.-B. Li, Y. Wang, J. Guo, D. Zhang, Z. Duan, *Nature* **2017**, *546*, 124-128.

[24] Q. H. Zhang, X. He, J. N. Shi, N. P. Lu, H. B. Li, Q. Yu, Z. Zhang, L. Q. Chen, B. Morris, Q. Xu, P. Yu, L. Gu, K. J. Jin, C. W. Nan, *Nat. Commun.* **2017**, *8*, 104.

[25] Q. Yang, H. J. Cho, H. Jeen, H. Ohta, *Adv. Mater. Interfaces* **2019**, *6*, 1901260.

[26] X. Qian, J. W. Zhou, G. Chen, *Nature Mater.* **2021**, *20*, 1188-1202.

[27] P. Gao, Z. C. Kang, W. Y. Fu, W. L. Wang, X. D. Bai, E. G. Wang, *J. Am. Chem. Soc.* **2010**, *132*, 4197-4201.

[28] H. J. Cho, Y. Takashima, Y. Nezu, T. Onozato, H. Ohta, *Adv. Mater. Interfaces* **2020**, *7*, 1901816.

[29] Y. Takashima, Y. Zhang, J. Wei, B. Feng, Y. Ikuhara, H. J. Cho, H. Ohta, *J. Mater. Chem. A* **2021**, *9*, 274-280.

[30] H. J. Cho, Y. Z. Wu, Y. Q. Zhang, B. Feng, M. Mikami, W. Shin, Y. Ikuhara, Y. M. Sheu, K. Saito, H. Ohta, *Adv. Mater. Interfaces* **2021**, *8*, 2001932.

Solid-state thermal transistor that controls heat flow with an on-to-off ratio of the thermal conductivity is ~4 without using any liquid is demonstrated. Upon turn on and off the thermal transistor by the electrochemical redox treatment in air, the crystal structure and the thermal conductivity of the $SrCoO_x$ layer are repeatedly modulated. This boosts solid-state thermal transistor development.

Q. Yang, H. J. Cho, Z. Bian, M. Yoshimura, J. Lee, H. Jeen, J. Lin, J. Wei, B. Feng, Y. Ikuhara, and H. Ohta*

Solid-State Electrochemical Thermal Transistors

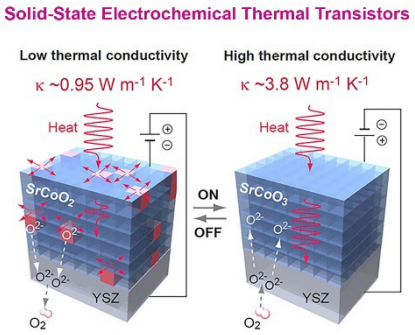

Supporting Information

Solid-State Electrochemical Thermal Transistors

*Qian Yang, Hai Jun Cho, Zhiping Bian, Mitsuki Yoshimura, Joonhyuk Lee, Hyoungjeen Jeen, Jinghuang Lin, Jiake Wei, Bin Feng, Yuichi Ikuhara, and Hiromichi Ohta**

Table of Contents

S1.1. Fabrication and electrochemical redox treatment of $SrCoO_{2.5}$/GDC bilayers on (001) YSZ single crystal substrates

Figure S1 illustrates the fabrication and electrochemical reduction/oxidation treatment of $SrCoO_{2.5}$ films, which involve four steps: film growth, electrode preparation, electrochemical reduction/oxidation of $SrCoO_{2.5}$, and electrode removal. **Step 1**: A $SrCoO_{2.5}$ film is heteroepitaxially grown on 10%-Gd-doped CeO_2 (GDC)-buffered (001)-oriented YSZ substrates by pulsed laser deposition (PLD) technique. First, ~10-nm-thick GDC is heteroepitaxially grown on YSZ (10 mm × 10 mm × 0.5 mm, double-sided polished, Crystal Base) substrate at 750 °C in an oxygen atmosphere (10 Pa). Focused KrF excimer laser pulses (λ = 248 nm, fluence ~2 J cm^{-2} pulse^{-1}, repetition rate = 10 Hz) are irradiated onto the ceramic target of GDC. Then a ~60-nm-thick $SrCoO_{2.5}$ film is heteroepitaxially grown on the GDC film at 750 °C in an oxygen atmosphere (10 Pa) with a laser fluence of ~2 J cm^{-2} pulse^{-1}. After film growth, the sample is cooled to room temperature in the PLD chamber in an oxygen atmosphere (10 Pa), yielding a brown film. **Step 2**: The sample is cut into four pieces (5 mm × 5 mm × 0.5 mm). Next, the electrodes are prepared. The film surface is mechanically pressed on an Au foil (ground electrode), and a small amount of Ag paste is applied on the back side of the YSZ substrate. The Ag paste is used as the gate electrode, and the Au foil is used as the ground electrode. **Step 3**: After heating the sample at 280 °C in air, a gate voltage of −8 V is applied to the Ag paste electrode for the electrochemical reduction of $SrCoO_{2.5}$ and that of +8 V for electrochemical oxidation of $SrCoO_{2.5}$. In both cases, the flown electron density is ~2 × 10^{22} cm^{-3}, which is sufficient for the electrochemical reduction of $SrCoO_{2.5}$ ($SrCoO_{2.5} + e^- \rightarrow SrCoO_2 + 0.5O^{2-}$, ~1.7 × 10^{22} cm^{-3}) and the electrochemical oxidation of $SrCoO_{2.5}$ ($SrCoO_{2.5} + 0.5O^{2-} \rightarrow SrCoO_3 + e^-$, ~1.7 × 10^{22} cm^{-3}). **Step 4**: The Ag paste electrode is mechanically removed. Reduction treatment produces a colorless and transparent film, whereas the oxidation treatment generates a black one.

S1.2. Crystal structure of the $SrCoO_x$ films

Figure S2 summarizes the out-of-plane XRD patterns of (a) as-grown, (b) oxidized, and (c) reduced samples. In the as-grown state (**Fig. S2a**), the intense diffraction peaks of 00*l* brownmillerite (BM) $SrCoO_{2.5}$ are seen together with 002 GDC and 002 YSZ (*), indicating that the $SrCoO_{2.5}$ films have a strong *c*-axis orientation. The full width at half maximum (FHWM) of the rocking curve of 008_{BM} is ~0.6°, supporting this conclusion. The in-plane XRD pattern (data not shown) shows that $SrCoO_{2.5}$ films are heteroepitaxially grown on (001) GDC / (001) YSZ substrates with the following relationship: (001)[110] $SrCoO_{2.5}$ || (001)[100] GDC/YSZ. After the electrochemical oxidation treatment (**Fig. S2b**), the 002_{BM}, 006_{BM}, and $00\underline{10}_{BM}$ peaks disappear, and the 001 and 002 diffraction peaks of perovskite (P) $SrCoO_3$ appear. The in-plane XRD pattern (data not shown) shows that the epitaxial relation is maintained. After the electrochemical reduction treatment (**Fig. S2c**), the out-of-plane and in-plane XRD patterns are similar to those of the oxidized one. Therefore, the reduced phase is assumed to be defect perovskite (DP).

Figure S3 shows the X-ray reflectivity (XRR) of the resultant films. According to the simulation, the as-grown $SrCoO_{2.5}$ film (**Fig. S3a**) is ~60 nm thick with a density of 5.18 g cm^{-3}, which corresponds well with the bulk value (5.18 g cm^{-3}). The estimated root mean square roughness is 0.52 nm, reflecting the topographic AFM image (**Fig. S4a**). The sharp streak of the RHEED pattern (**Fig. S4b**) also supports this conclusion. Neither oxidation (**Fig. S3b**) nor reduction (**Fig. S3c**) treatment results in a significant change, suggesting that topotactic oxidation and reduction occur.

S1.3. Optical and electrical properties of the $SrCoO_x$ films

Figure S5 shows the optical absorption spectra of the $SrCoO_x$ films at room temperature. The as-grown $SrCoO_{2.5}$ film, the oxidized $SrCoO_3$ film, and the reduced $SrCoO_2$ film are brown, black, and colorless and transparent, respectively (**right, inset**). The absorption of the as-grown $SrCoO_{2.5}$ film starts to increase when the photon energy exceeds ~0.4 eV due to the bandgap (d–d transition). The oxidized $SrCoO_3$ film absorbs photons in all ranges due to its metallic nature. By contrast, the reduced $SrCoO_2$ film does not absorb visible light (400–780 nm in wavelength). Consequently, it looks colorless and transparent. The direct bandgap (E_g) is ~3.1 eV, which is slightly larger than those of CoO (~2.8 eV, Co^{2+}) and $HSrCoO_{2.5}$ (~2.84 eV, Co^{2+})[1].

Then we measured the electrical properties of the $SrCoO_x$ films at room temperature. The electrical resistivity (ρ) and thermopower (S) of the as-grown $SrCoO_{2.5}$ film are ~0.97 Ω cm and +47 μV K^{-1}, respectively. After the oxidation treatment, ρ dramatically decreases to ~1.7 mΩ cm and S changes to −8 μV K^{-1}, showing the metallic electrical properties of the $SrCoO_3$ film. On the other hand, ρ and S of the reduced $SrCoO_2$ film are not obtained due to its insulating nature.

S1.4. Valence states of Co in the $SrCoO_x$ films

To further clarify the valence state of the Co ions, we conducted the soft X-ray absorption (XAS) measurements. The Co L_3-edges for the as-grown, oxidized, and reduced samples exhibit almost identical features with characteristic peaks at ~780.10 eV, 780.50 eV, and 779.10 eV, respectively (**Fig. S6a**). Compared to the reported XAS spectra of BM-$SrCoO_{2.5}$[2], PV-$SrCoO_3$[2], and CoO[3], the valence states of Co are +3, mostly +4, and +2 for the as-grown, oxidized, and reduced samples, respectively. Furthermore, the O K-edges of the as-grown sample show distinct differences from the other two samples in the range of 525–530 eV (**Fig. S6b**), indicating that hybridization between the O 2p orbital and the Co 3d orbital is suppressed when reduced. This is similar to the p–d hybridization feature of $HSrCoO_{2.5}$ (Co^{2+}) reported by Lu *et al*.[1] From these results, we conclude that the valence state of Co ion in the $SrCoO_2$ phase is +2.

S1.5. Summary

Table S1 summarizes the lattice parameters and electron transport properties of the $SrCoO_x$ films.

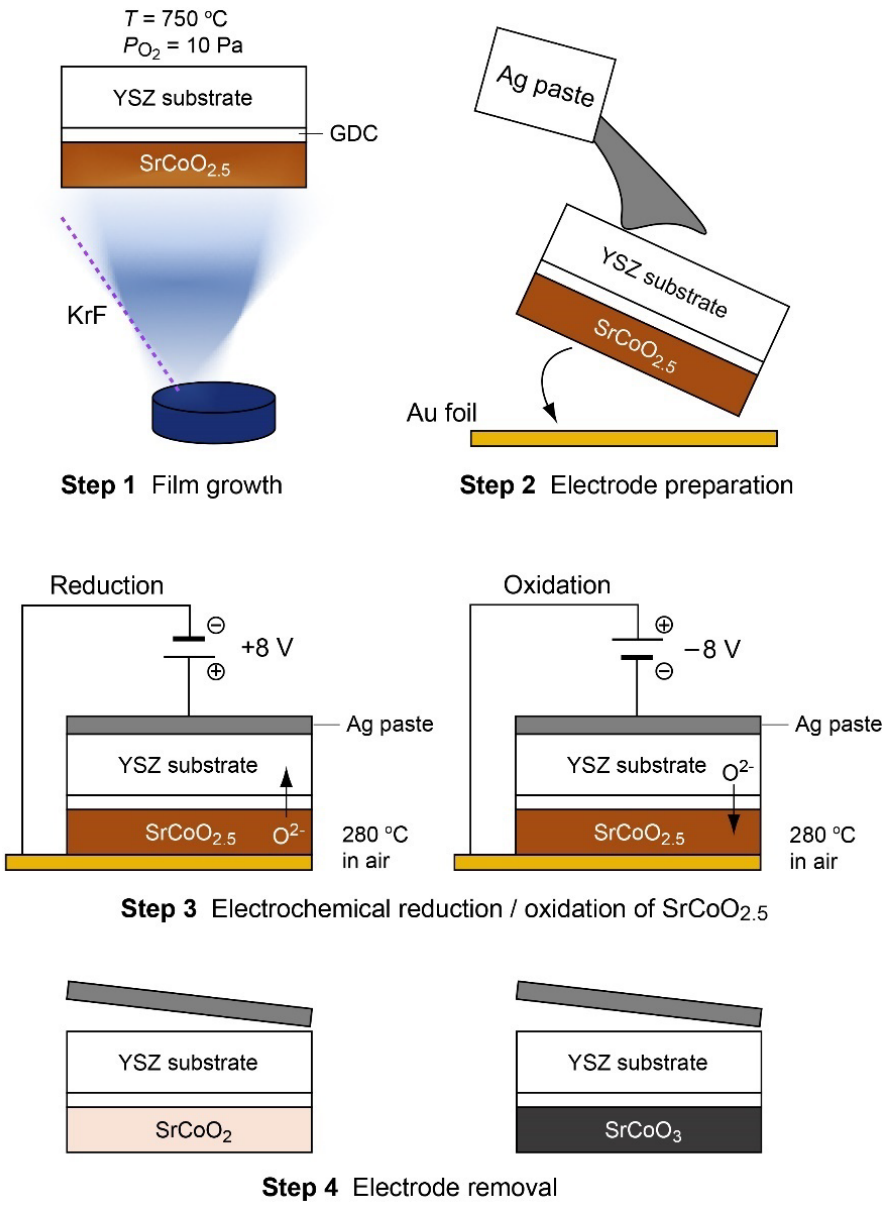

Figure S1. Fabrication and electrochemical reduction/oxidation treatment of $SrCoO_{2.5}$ films. **Step 1**: Film growth. **Step 2**: Electrode preparation. **Step 3**: Electrochemical reduction/oxidation of $SrCoO_{2.5}$. **Step 4**: Electrode removal. See the supplementary text for details of each step.

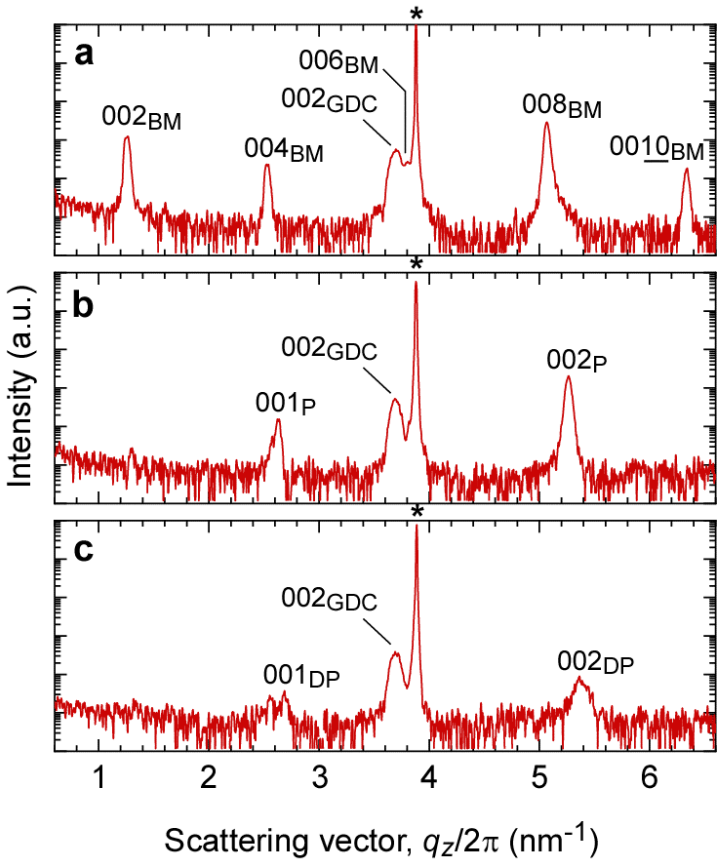

Figure S2. Out-of-plane X-ray diffraction patterns of the $SrCoO_x$/GDC bilayer films grown on (001) YSZ substrate. a) As-grown sample shows intense diffraction peaks of 00*l* brownmillerite (BM) $SrCoO_{2.5}$ together with 002 GDC and 002 YSZ (*). b) Oxidized $SrCoO_3$. Electrochemical oxidation treatment produces the 001 and 002 diffraction peaks of perovskite (P) $SrCoO_3$ and 002 GDC and 002 YSZ (*). c, Reduced $SrCoO_2$. Electrochemical reduction gives the 001 and 002 diffraction peaks of defect perovskite (DP) together with 002 GDC and 002 YSZ (*).

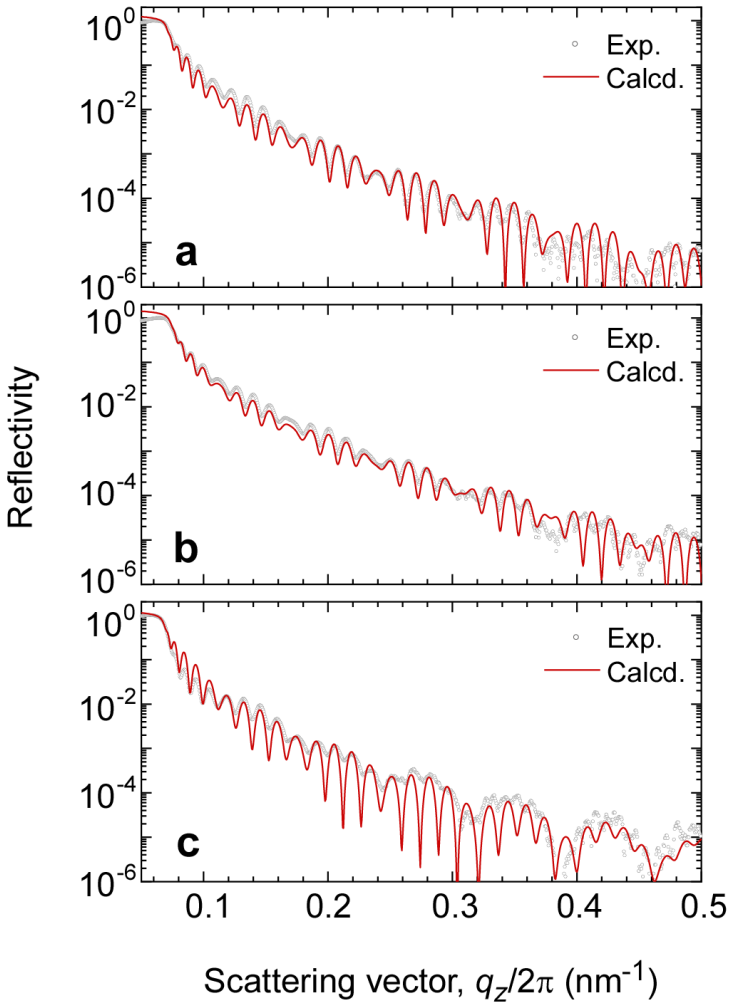

Figure S3. X-ray reflectivity of the $SrCoO_x$/GDC bilayer films grown on a (001) YSZ substrate. a) As-grown $SrCoO_{2.5}$. b) Oxidized $SrCoO_3$. c, Reduced $SrCoO_2$. Using the least square fitting, the thicknesses of $SrCoO_{2.5}$ and GDC layers are calculated as 61 nm and 13 nm, respectively. Neither the oxidation nor reduction treatments induce a significant change, suggesting that topotactic oxidation and reduction occur. Calculated density, thickness, and roughness are listed below.

a) As-grown $SrCoO_{2.5}$

Layer	Density (g cm^{-3})	Thickness (nm)	Roughness (nm)
$SrCoO_{2.5}$	5.18	61	0.63
GDC	7.21	13	0.35
YSZ	6.05		

b) Oxidized $SrCoO_3$

Layer	Density (g cm^{-3})	Thickness (nm)	Roughness (nm)
$SrCoO_3$	5.64	59	0.54
GDC	7.21	13	0.35
YSZ	6.05		

c) Reduced $SrCoO_2$

Layer	Density (g cm^{-3})	Thickness (nm)	Roughness (nm)
$SrCoO_2$	4.85	62	0.81

GDC	7.21	13	0.35
YSZ	6.05		

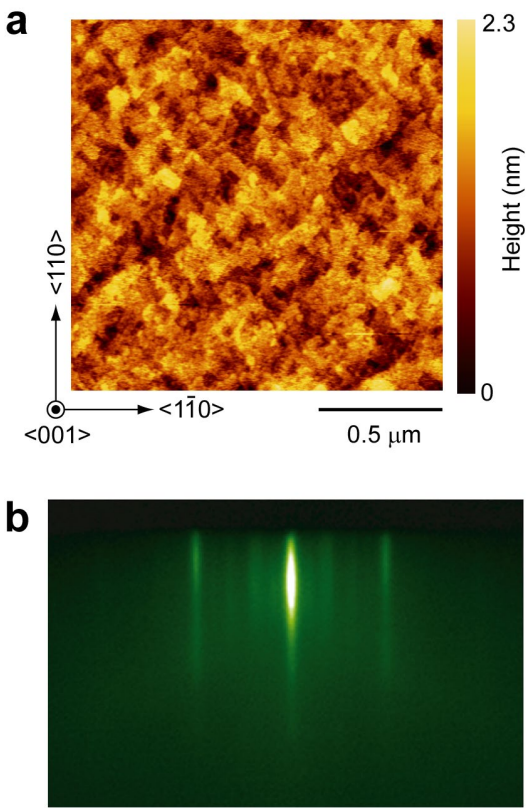

Figure S4. Surface morphology of the as-grown $SrCoO_{2.5}$ film. a) Topographic AFM image of the film shows a rather smooth surface composed of square-shaped patterns. b) RHEED pattern at the [110] azimuth. Intense streak pattern indicates that heteroepitaxial growth of $SrCoO_{2.5}$ occurs while maintaining a smooth surface.

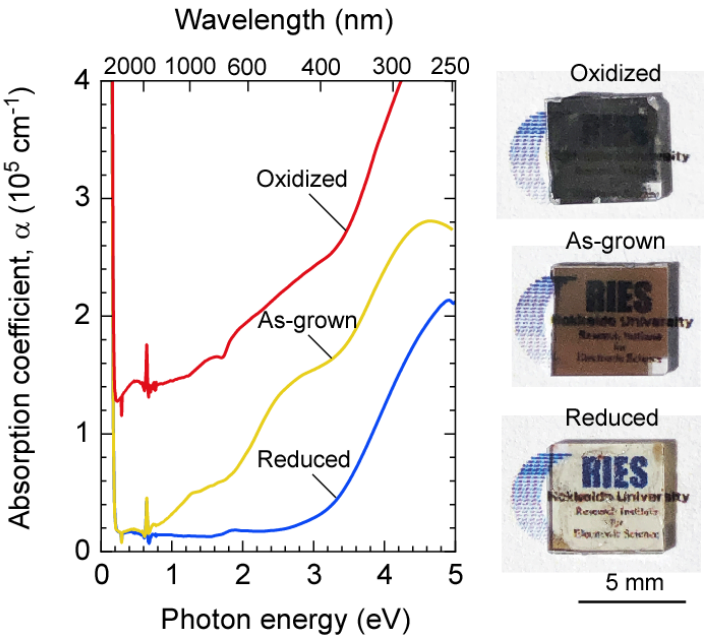

Figure S5. Optical absorption spectra. Absorption of the brown as-grown $SrCoO_{2.5}$ film starts to increase when the photon energy exceeds ~0.4 eV due to the bandgap (d–d transition). Black oxidized $SrCoO_3$ film absorbs photons in all ranges due to its metallic nature. By contrast, the colorless and transparent reduced $SrCoO_2$ film does not absorb visible light (400−780 nm in wavelength). Direct bandgap (E_g) of the reduced $SrCoO_2$ film is ~3.1 eV.

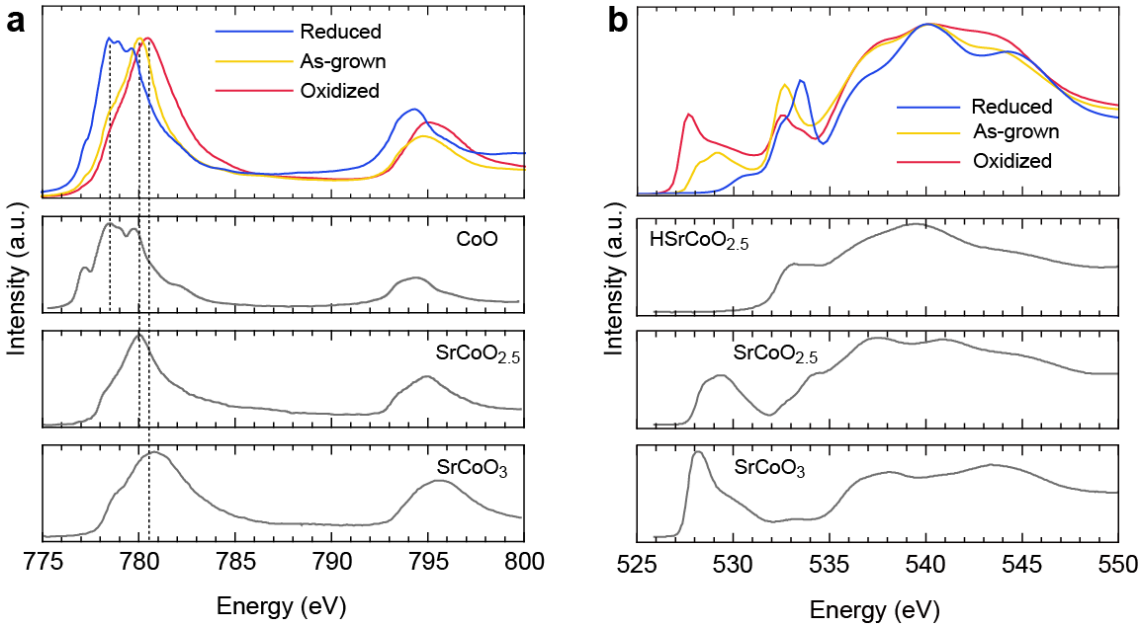

Figure S6. Valence states of Co in the $SrCoO_x$ films. Soft X-ray absorption spectra of (a) the Co $L_{2,3}$-edge and (b) the O K-edge. Co L_2-edge XAS spectra of the as-grown and oxidized samples are similar to those of $SrCoO_{2.5}$ and $SrCoO_3$ reported by Jeen *et al*.[2] O K-edge spectra of the as-grown and oxidized samples are also similar to those of $SrCoO_{2.5}$ and $SrCoO_3$ reported by Lu *et al*.[1] By contrast, the Co L_2-edge XAS spectrum of the reduced sample is similar to that of CoO reported by Indra *et al*.[3], indicating that the valence state of Co ion is +2. O K-edge spectrum of the reduced sample should reflect the existence of Co^{2+}.

Table S1. Lattice parameters and electron transport properties of the $SrCoO_x$ films. Lattice parameters are calculated from the 00*l* diffraction peaks in the out-of-plane XRD patterns and the 220 diffraction peaks in the in-plane XRD patterns (assuming a square lattice). Electron transport properties of the as-grown $SrCoO_{2.5}$ and oxidized $SrCoO_3$ are similar to those of our previous report[4], whereas those of the reduced $SrCoO_2$ are not measured due to its highly insulating nature.

	Lattice parameters	Resistivity (Ω cm)	Thermopower (μV K^{-1})
As-grown $SrCoO_{2.5}$	a = 0.3872 nm c = 0.3860 nm	0.97 *cf*. 4.0 (Ref. [4])	+47 *cf*. +70 (Ref. [4])
Oxidized $SrCoO_3$	a = 0.3862 nm c = 0.3802 nm	1.7×10^{-3} *cf*. 0.7×10^{-3} (Ref. [4])	−8 *cf*. −0.5 (Ref. [4])
Reduced $SrCoO_2$	a = 0.3826 nm c = 0.3732 nm	(Highly insulating)	(Highly insulating)

S2. Fabrication of the thermal transistors

$SrCoO_{2.5}$ films were heteroepitaxially grown on 10%-Gd-doped CeO_2 (GDC) buffered (001)-oriented YSZ substrates by pulsed laser deposition (PLD) technique. First, ~10-nm-thick GDC was heteroepitaxially grown on a YSZ (10 mm × 10 mm × 0.5 mm, double-sided polished, Crystal Base) substrate at 750 °C in an oxygen atmosphere (10 Pa). Focused KrF excimer laser pulses (λ = 248 nm, fluence ~2 J cm^{-2} $pulse^{-1}$, repetition rate = 10 Hz) were irradiated onto the ceramic target of GDC. Subsequently, a ~50-nm-thick $SrCoO_{2.5}$ film was heteroepitaxially grown on the GDC film at 750 °C in an oxygen atmosphere (10 Pa). The laser fluence was ~2 J cm^{-2} $pulse^{-1}$. After film growth, the sample was cooled to room temperature in the PLD chamber in an oxygen atmosphere (10 Pa). Then ~60-nm-thick Pt film was sputtered on the top surface of the $SrCoO_{2.5}$ epitaxial film followed by ~40-nm-thick Pt film sputtering on the backside of the YSZ substrate. Pt sputtering was performed at room temperature. Finally, the sample was cut into four squares (5 mm × 5 mm).

The multilayer structure and atomic arrangement of switching devices were visualized using scanning transmission electron microscopy (STEM, JEM-ARM200CF, JEOL) operating at 200 keV. **Figure S7** shows the STEM image and energy dispersive spectroscopy (EDS) mapping of each element for a device. A multilayer structure composed of Pt, $SrCoO_{2.5}$, GDC, and YSZ was clearly visualized. **Figure S8** shows the cross-sectional STEM images of the as-fabricated $SrCoO_{2.5}$ layer. The brownmillerite structure $SrCoO_{2.5}$ crystal is clearly visualized.

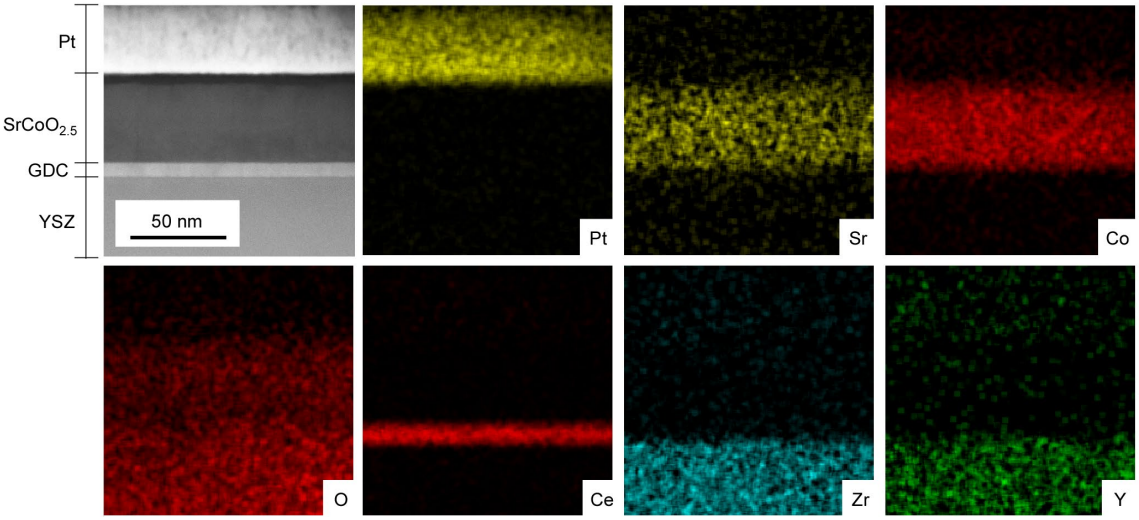

Figure S7. STEM analyses of the switching device in the as-fabricated state. Multilayered structure composed of Pt, $SrCoO_{2.5}$, GDC, and YSZ is clearly observed.

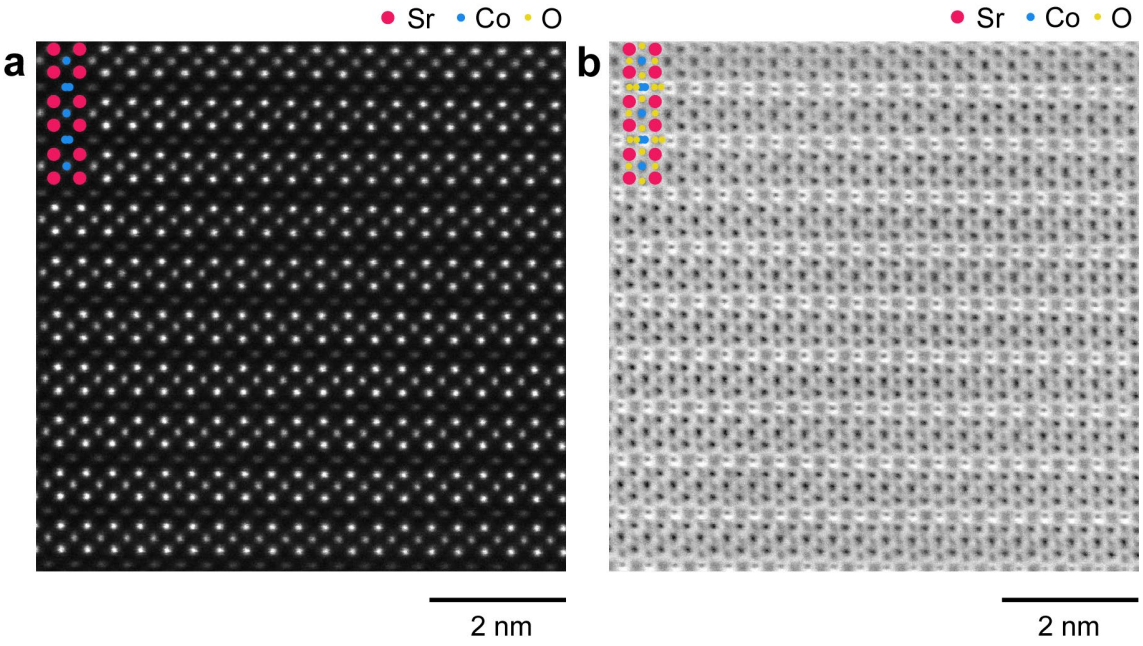

Figure S8. Cross-sectional STEM images of the as-fabricated $SrCoO_{2.5}$. (a) HAADF-STEM image shows that the heavier atomic column has a brighter contrast. Brighter dots are Sr (atomic number, $Z = 38$) and darker dots are Co ($Z = 27$). (b) ABF-STEM image to visualize lighter atoms. In addition to the Sr and Co columns, the O column is clearly visualized. This structure belongs to the brownmillerite structure.

S3. Detailed thermal transistor operations

As shown in **Fig. S9**, a thermal transistor (5 mm × 5 mm) was put on a Pt-coated glass substrate, which was heated at 280 °C in air. Then the electrochemical redox treatment was performed by applying a constant current of ±50 μA. The current application time controlled the reduction/oxidation degrees. After applying the current, the sample was immediately cooled to room temperature.

The oxide ion conductivity of the YSZ single crystal substrate is 2 μS cm^{-1} at 280 °C (**Fig. S10**), and the Arrhenius plot shows a linear relationship. The resistance of the substrate (5 mm × 5 mm × 0.5 mm) is ~100 kΩ at 280 °C. This resistance dominates the overall voltage for the redox reaction.

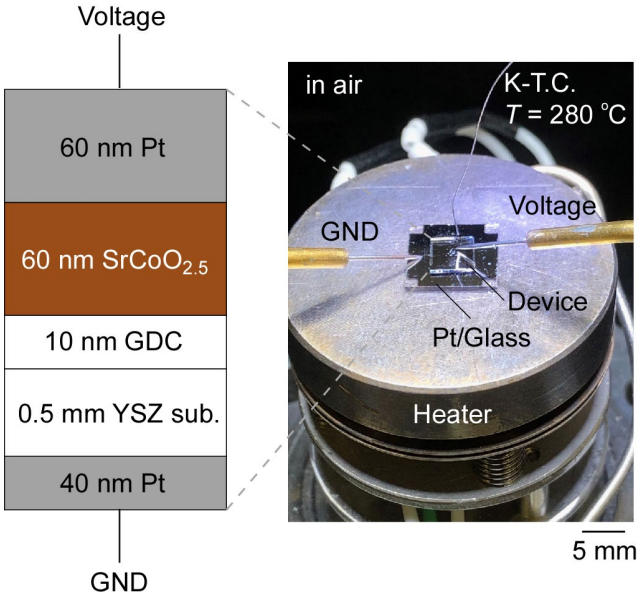

Figure S9. Operation of a solid-state electrochemical thermal transistor. Thermal transistor is composed of ~60-nm-thick Pt film, ~60-nm-thick $SrCoO_{2.5}$ film, ~10-nm-thick Gd-doped CeO_2 (GDC) film, 0.5-mm-thick (001) YSZ single crystal substrate, and 40-nm-thick Pt film. Device is placed on a Pt-coated glass substrate and heated at 280 °C in air. K-type thermocouple (T.C.) is used to monitor the surface temperature of the transistor. Device size is 5 mm × 5 mm, and a negative current (−50 μA) is applied for the reduction and a positive current (+50 μA) for oxidation.

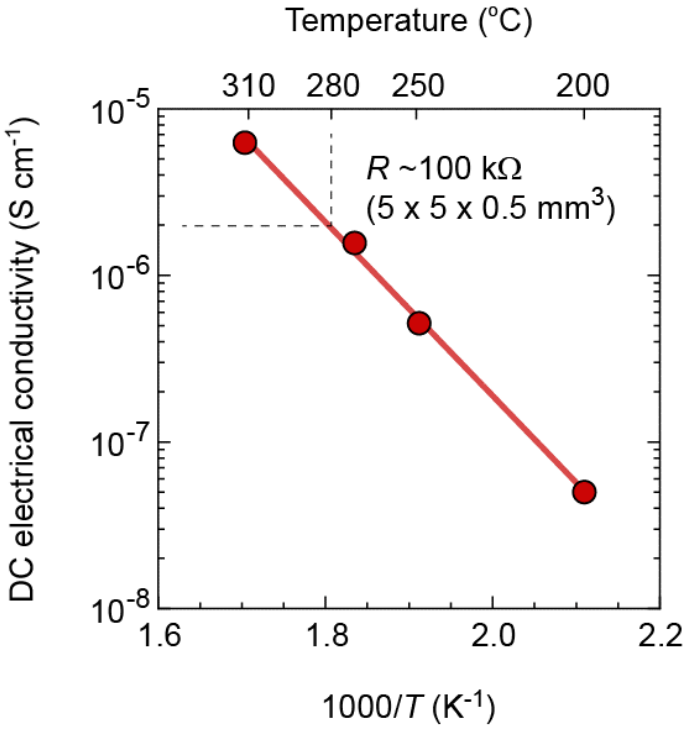

Figure S10. DC electrical conductivity of the YSZ single crystal substrate. At 280 °C, the dc electrical resistance (R) of the YSZ substrate (5 mm × 5 mm × 0.5 mm) is ~100 kΩ. Temperature dependence of the dc electrical conductivity is similar to that reported previously.[5, 6]

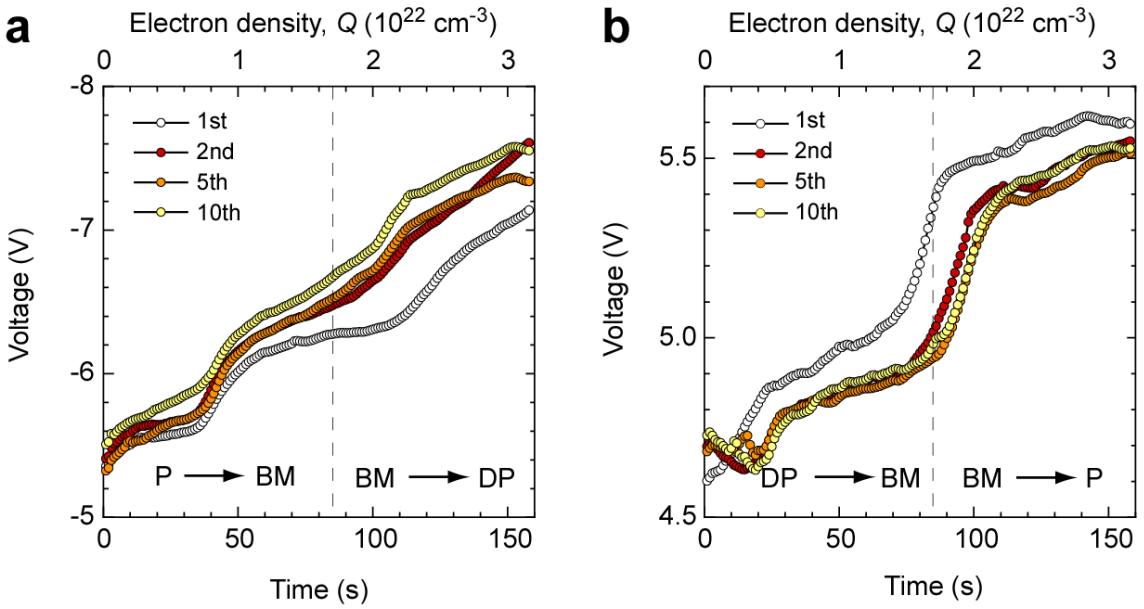

Figure S11. Changes in the required dc voltage of the switching device during (a) reduction from $SrCoO_3$ to $SrCoO_2$ and (b) oxidation from $SrCoO_2$ to $SrCoO_3$ upon cycling. Dotted lines indicate the theoretical electron density for the redox reaction of $SrCoO_3/SrCoO_2$ or $SrCoO_2/SrCoO_3$ (Q ~1.7 × 10^{22} cm^{-3}). Applied voltage is almost unchanged in each redox cycles, except for the first reduction and oxidation treatments.

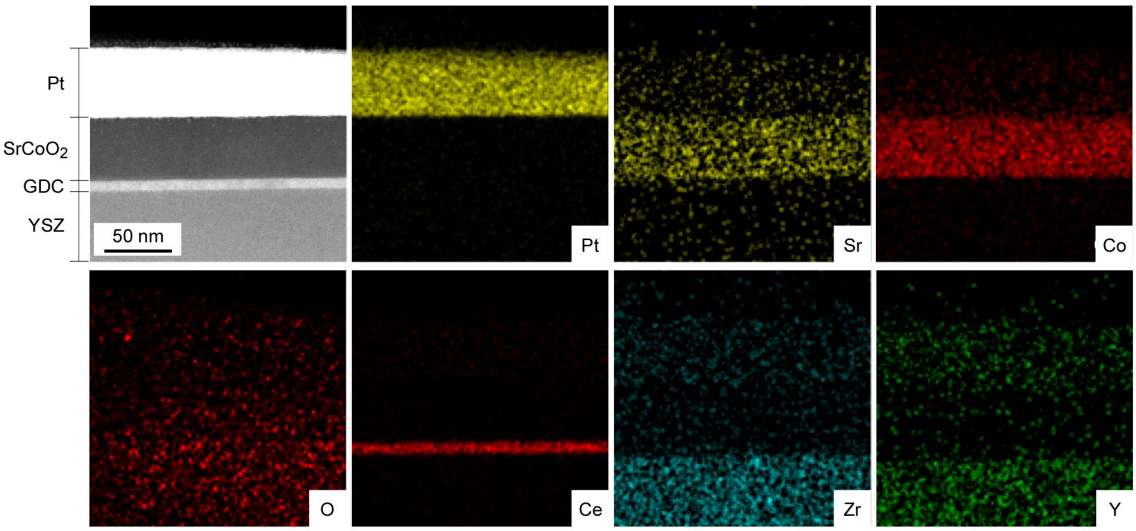

Figure S12. STEM analyses of the switching device in the reduced state. Multilayered structure composed of Pt, $SrCoO_2$, GDC, and YSZ is clearly observed.

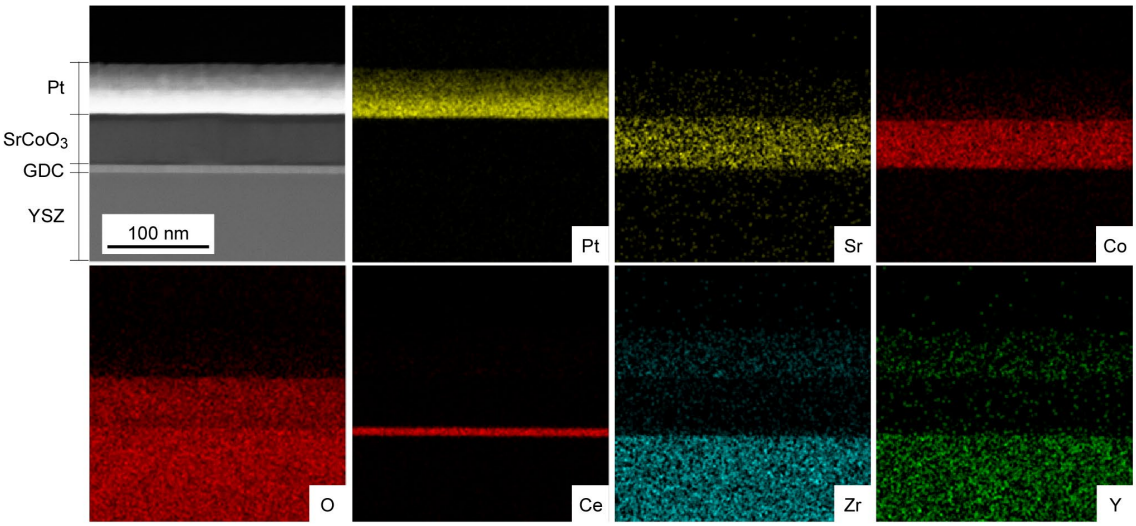

Figure S13. STEM analyses of the switching device in the oxidized state. Multilayered structure composed of Pt, $SrCoO_3$, GDC, and YSZ is clearly observed.

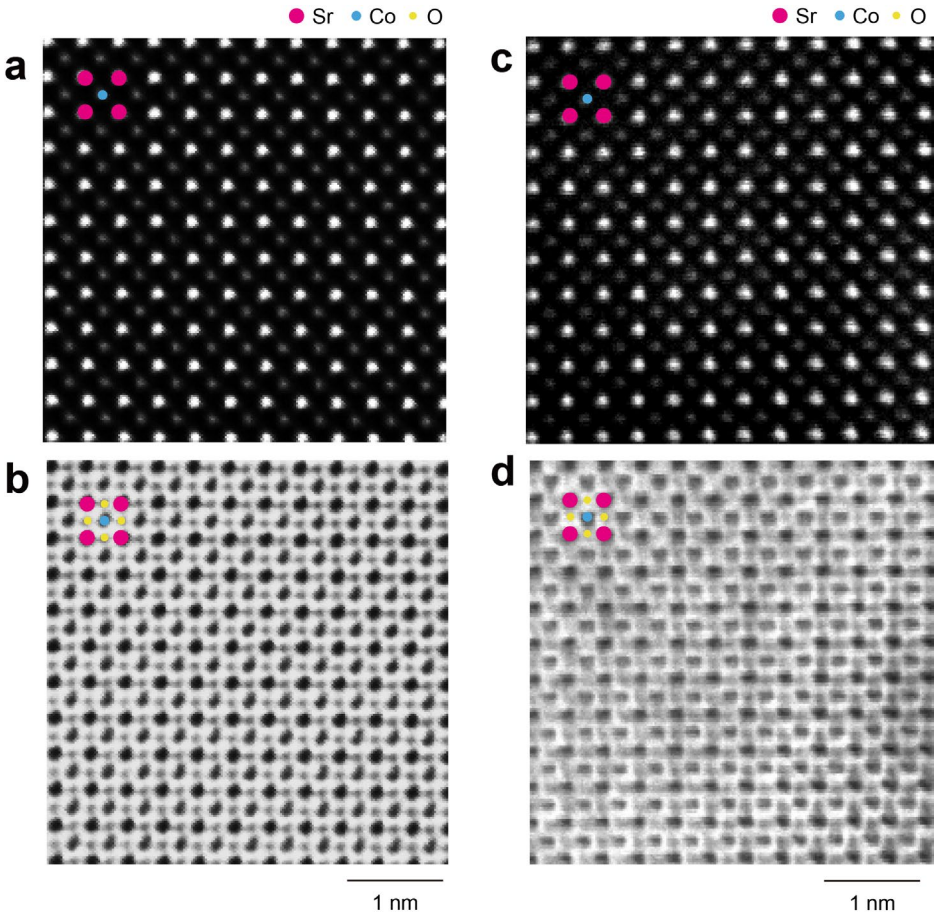

Figure S14. Cross-sectional STEM images of (a, b) the oxidized $SrCoO_3$ and (c, d) the reduced $SrCoO_2$. (a, c) HAADF-STEM images show that the heavier atomic column has a brighter contrast. Square lattice composed of Sr and Co is clearly visualized. Brighter dots are Sr (atomic number, $Z = 38$) and darker dots are Co ($Z = 27$). (b, d) ABF-STEM images to visualize lighter atoms. In addition to the Sr and Co columns, the O column is clearly visualized. This structure belongs to the perovskite structure but contains randomly distributed oxygen defects. Thus, both the oxidized $SrCoO_3$ and the reduced $SrCoO_2$ have a perovskite structure.

S4. Thermal conductivity measurement of the thermal transistors

The thermal conductivity of the thermal transistors in the cross-plane direction was measured by the time domain thermoreflectance (TDTR) method at room temperature. We used commercially available TDTR equipment (PicoTR, PicoTherm Co.[7]). **Figure S15** shows the schematic optical circuit of the TDTR equipment. The setup is so-called front heating/front detection mode-mirror image method. Sputtered Pt films (thickness: ≈60 nm) were used as a transducer. The samples were irradiated with femtosecond laser pulses (wavelength: 1550 nm; pulse duration: 0.5 ps), and the change in the reflectivity in the time domain was recorded with a probe laser (wavelength: 775 nm; pulse duration: 0.5 ps) (**Fig. S16**). Other specs of the lasers are listed in **Table S2**.

The obtained thermoreflectance phase signals (**Figs. S17** and **S18**) were analyzed with a software package provided by the manufacturer (PicoTherm Co.[7]) using the physical properties listed in **Table S3**. We assumed that the specific heat capacity (C_p) of $SrCoO_x$ is always 485 J kg^{-1} K^{-1} and it is independent on x. Since κ of GDC is similar to YSZ, we regarded GDC/YSZ as one layer. Further, the interfacial thermal resistance between the 2nd layer and the 3rd layer was fixed at 4×10^{-13} m^2 K W^{-1} (= negligible). We calculated the thermal conductivity of the 2nd layer. The interfacial thermal resistance between the 1st and the 2nd layer was ~3×10^{-9} m^2 K W^{-1} and it did not show the oxidized or reduced state dependence. This value is comparable to that measured Pt/oxide single crystal such as $LiNbO_3$ (2×10^{-9} m^2 K W^{-1}) and LSAT (2×10^{-9} m^2 K W^{-1}) that the thermal conductivity is known (data not shown).

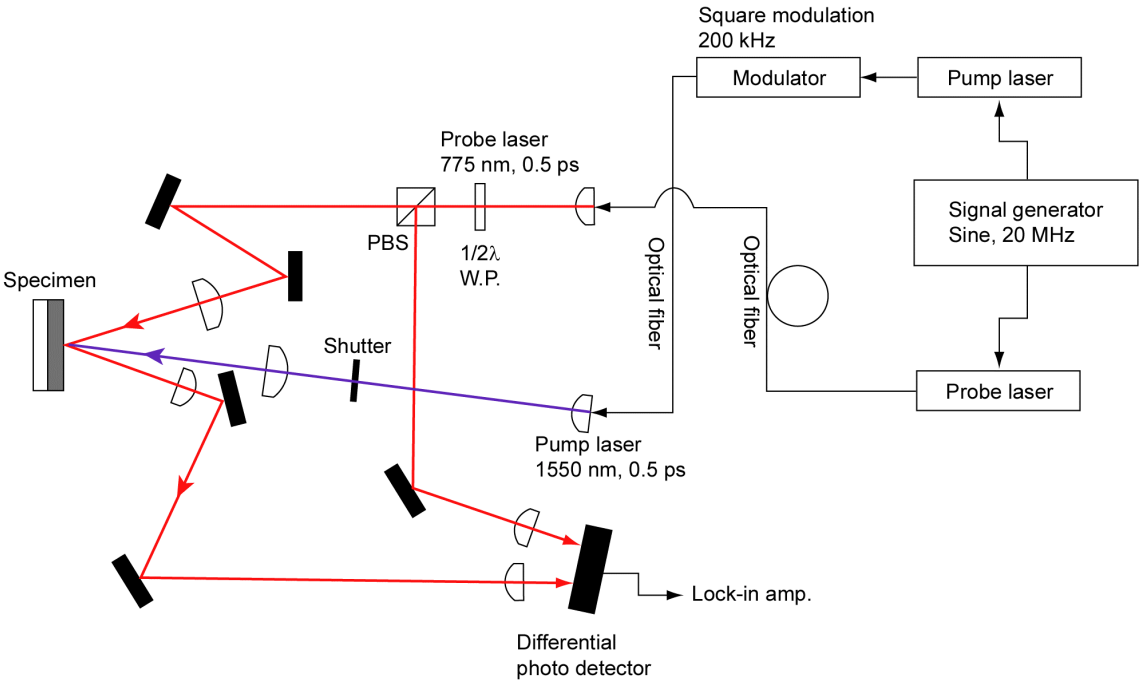

Figure S15. Schematic optical circuit of the TDTR system (PicoTR, PicoTherm). With picosecond thermoreflectance analyzer PicoTR, laser pulses (pump laser) of 0.5 ps pulse width are applied to the sample with the time period of 50 ns. The temperature response is detected with the probe laser. (https://analyzing-testing.netzsch.com/en/products/time-domain-thermoreflectance-analyzer-tdta/nanotr-picotr)

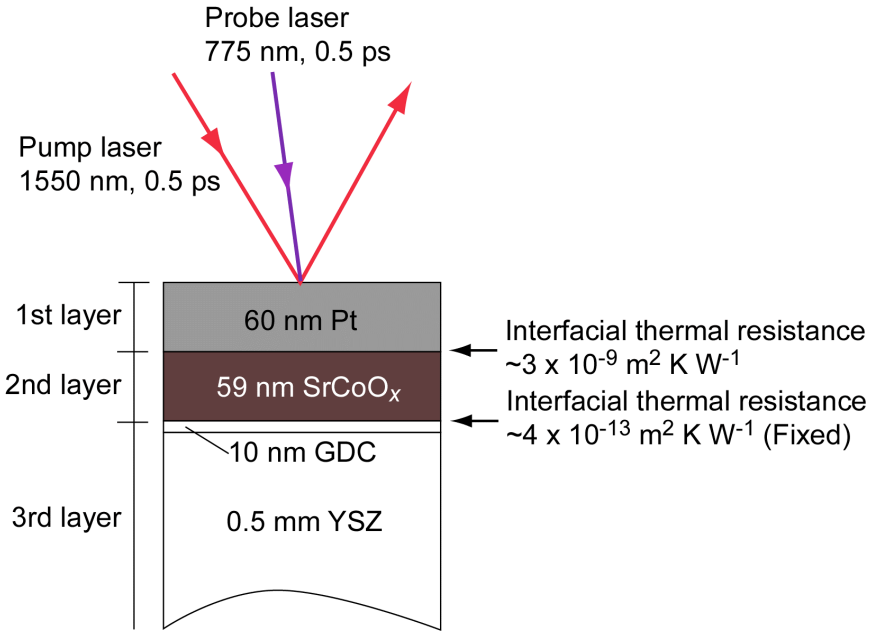

Figure S16. Schematic experimental setup of the TDTR measurement of the thermal transistors.

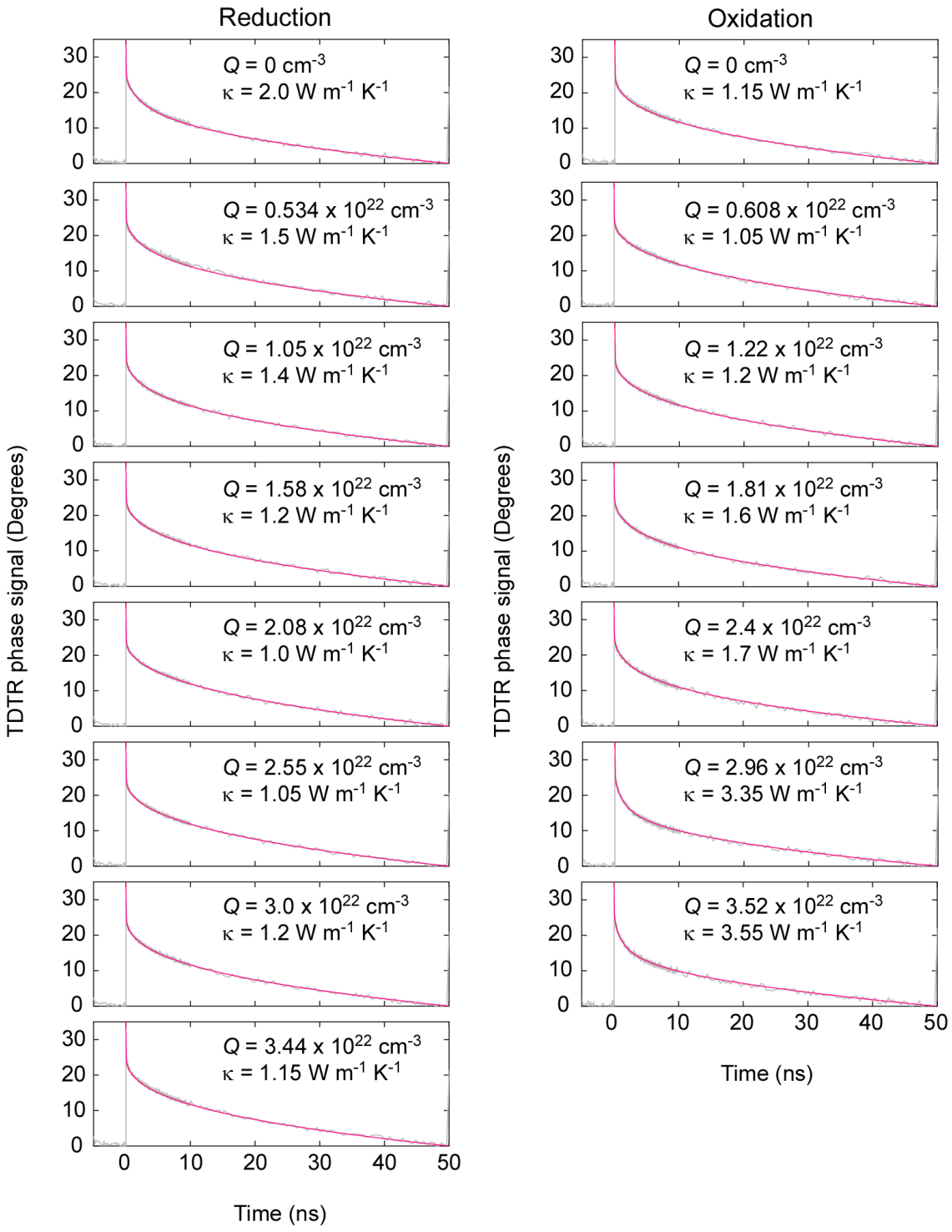

Figure S17. TDTR fitting results for **Figures 2c** and **2f**. Gray: observed, pink: simulated.

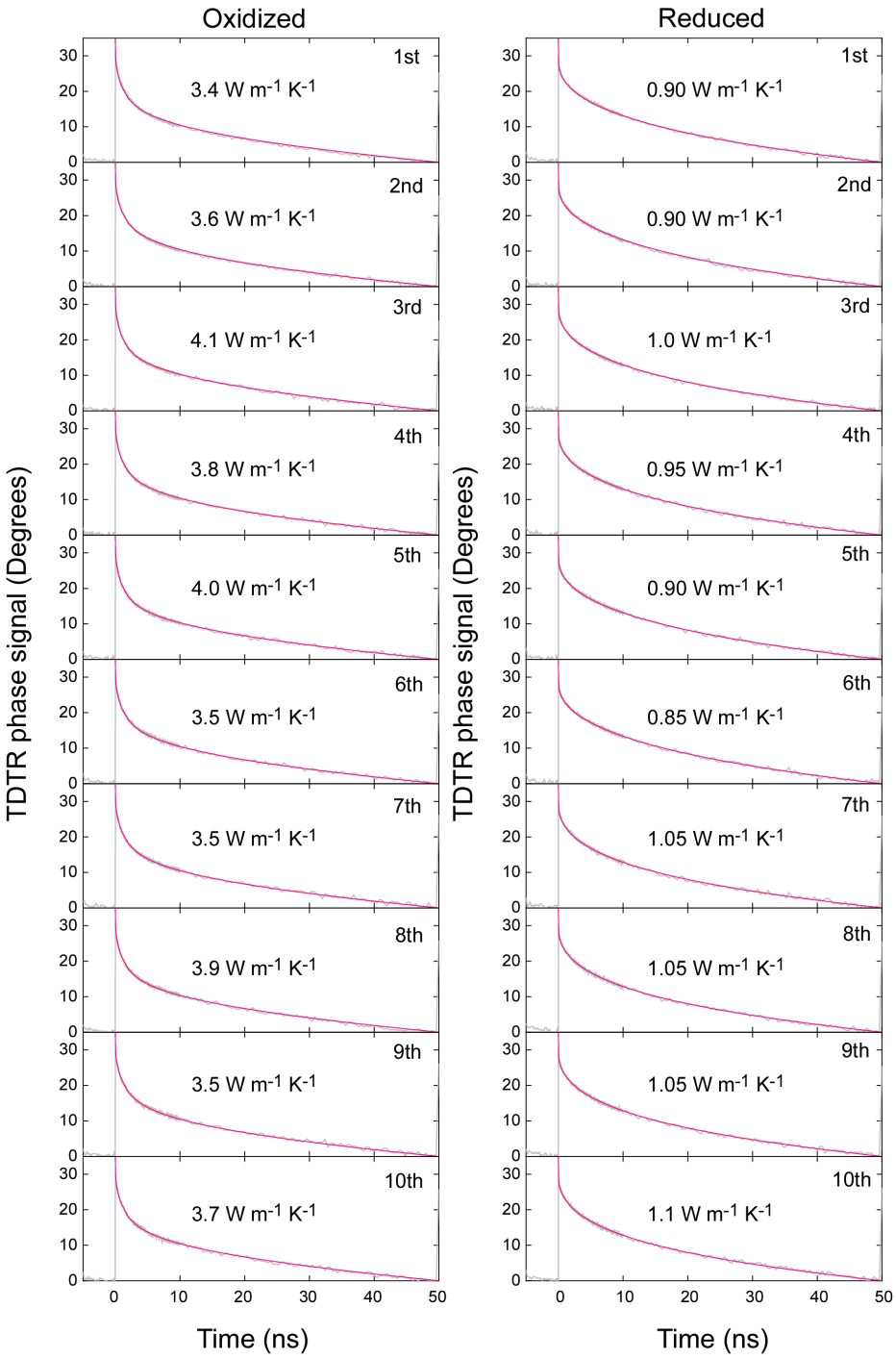

Figure S18. TDTR fitting results for **Figure 5b**. Gray: observed, pink: simulated.

Table S2. Spec list of the lasers that are used in the TDTR equipment.

Pump laser

Wavelength (nm)	1550
Repetition rate (MHz)	20
Spot size (μm)	45
Modulation frequency (kHz)	200

Probe laser

Wavelength (nm)	775
Repetition rate (MHz)	20
Spot size (μm)	25
Modulation frequency (kHz)	None (only pump laser)

Table S3. List of the physical properties that used for the TDTR simulation. We assumed that the specific heat capacity (C_p) of $SrCoO_x$ is independent on x. Since κ of GDC is similar to YSZ, we regarded GDC/YSZ as one layer. Further, the interfacial thermal resistance between the 2nd layer and the 3rd layer was fixed at 4×10^{-13} m^2 K W^{-1} (= negligible). We calculated the thermal conductivity of the 2nd layer. The interfacial thermal resistance between the 1st and the 2nd layer was ~3×10^{-9} m^2 K W^{-1} and it did not show the oxidized or reduced state dependence.

	First layer	Second layer	Third layer
Materials	Pt	$SrCoO_x$	GDC/YSZ
C_p (J kg^{-1} K^{-1})	132	485	460
Density (kg m^{-3})	21228	5180	6050
κ (W m^{-1} K^{-1})	45	Calculated	1.6
Thickness (m)	5.99×10^{-8}	5.92×10^{-8}	-------

References

[1] N. Lu, P. Zhang, Q. Zhang, R. Qiao, Q. He, H.-B. Li, Y. Wang, J. Guo, D. Zhang, Z. Duan, *Nature* **2017**, *546*, 124-128.
[2] H. Jeen, W. S. Choi, M. D. Biegalski, C. M. Folkman, I. C. Tung, D. D. Fong, J. W. Freeland, D. Shin, H. Ohta, M. F. Chisholm, H. N. Lee, *Nature Mater.* **2013**, *12*, 1057-1063.
[3] A. Indra, P. W. Menezes, C. Das, C. Gobel, M. Tallarida, D. Schmeisser, M. Driess, *J. Mater. Chem. A* **2017**, *5*, 5171-5177.
[4] Q. Yang, H. J. Cho, H. Jeen, H. Ohta, *Adv. Mater. Interfaces* **2019**, *6*, 1901260.
[5] S. Ikeda, O. Sakurai, K. Uematsu, N. Mizutani, M. Kato, *J. Mater. Sci.* **1985**, *20*, 4593-4600.
[6] S. P. S. Badwal, *J. Mater. Sci.* **1984**, *19*, 1767-1776.
[7] S. H. Firoz, T. Yagi, N. Taketoshi, K. Ishikawa, T. Baba, *Meas. Sci. Technol.* **2011**, *22*, 024012.